METROLOGY BENCH

by

Prashanth Jaganmohan

A thesis submitted to the faculty of
The University of North Carolina at Charlotte
in partial fulfillment of the requirements
for the degree of Master of Science in
Mechanical Engineering

Charlotte

2017

Approved by:

_____
Dr. Edward Morse

_____
Dr. Jimmie Miller

_____
Dr. Gert Goch

ABSTRACT

PRASHANTH JAGANMOHAN. Metrology bench. (Under the direction of DR. EDWARD MORSE)

Portable large scale metrology instruments continue to gain popularity due to their increasing use in industrial applications. As a result, it has become more and more crucial to develop reliable large scale artifacts or other large scale equipment to evaluate and verify the performance of such instruments. The work described in this research involves the design and construction of such a piece of equipment, namely a metrology bench consisting of a rail-carriage system for the purposes of calibration of artifacts including scale bars, tapes and performance evaluation of commercial large scale metrology instruments such as laser trackers. This work also demonstrates the use of the bench for applications including ball bar calibration and evaluation of interferometric ranging capability of a laser tracker by comparison against a reference interferometer. The conventional methodology of a back-to-back ranging test presented by the National Institute of Standards and Technology (NIST) has been modified to eliminate some sources of uncertainty. Further, an alternative approach is introduced for a common-path test method presented by NIST. This approach is believed to ease setup and lower the cost. Several environmental sensors have been integrated into the bench system to enable effective thermal compensation and this is shown to improve measurement results. Uncertainty analyses have been carried out to study the influence of the bench properties, among other contributing factors, on the measured quantities, and the varying trends of these uncertainties are brought out.

DEDICATION

This thesis is dedicated to my parents and my grandmother for their extraordinary encouragement and support.

ACKNOWLEDGEMENTS

TABLE OF CONTENTS

LIST OF TABLES

LIST OF FIGURES

CHAPTER 1: INTRODUCTION

Large scale metrology instruments are known to have large measurement volumes over which the instrument measurement errors are specified by manufacturers. Verifying the performance of such instruments would therefore require long calibrated reference lengths. These reference lengths could be of the form of fixed length artifacts such as scale bars which have target nests at each end designed to hold spherically mounted retroreflectors (SMRs). In such a case, realization of different reference lengths would be expensive and also difficult to manufacture, resulting in the verification process to be cumbersome. On the other hand, reference lengths can also be of the virtual type, where there is no solid material connecting the two ends directly. Such virtual lengths are often achieved by positioning two individual nests at different locations using rigid supporting structures such as tripods. The two nests would then constitute a virtual reference length since there is no scale bar directly connecting the two nests, but rather, the metrology loop is completed through the structure of the tripods and the ground. Moving the tripods relative to each other would then result in producing virtual reference lengths of different desired lengths. This would eliminate the need to manufacture different artifacts for each desired reference length. However, the metrology loop is completed through the ground, which, in most cases, possesses thermal expansion properties that are not always consistent and therefore may not be easy to predict. Thus it is desirable to have a more thermally stable material having well defined thermal properties serve as the material that defines the

separation between the two points that constitute the reference length. In general, a reference length can be realized using either a physical stable length or a continuously monitored length. The latter can be achieved using a rail-carriage system, where a rail of suitable material with desirable thermal properties is chosen and two nests with SMRs can be fixed at different positions along the rail. The distance between the two SMRs can then be interferometrically calibrated using a stable linear reference interferometer. Such a continuously monitored length will only require stability over the time taken to read the length from the reference laser. Rather than fixing the nests directly to the rail, the use of movable carts with nests fixed on them, would allow room for more flexibility. These were the design intentions behind creating a metrology bench consisting of a rail-carriage system.

The primary applications for which it was desired to have such a metrology bench included in-house calibration of reference lengths such as ball bars, creation and realization of custom reference lengths, calibration of tape measures and also for performance verification of commercial large scale metrology equipment such as laser trackers.

Laser trackers are portable coordinate measuring machines that utilize a spherical coordinate system to measure the location of points in three dimensional space. In other words, a point's coordinates are reported by a laser tracker in terms of three parameters, namely a range (radial distance to the point), azimuthal angle (horizontal angle) and zenith angle (vertical angle). The range can be reported by interferometry (IFM) or Absolute Distance Measurement (ADM) or both, depending on the manufacturer and the model. The horizontal and vertical angles are measured by two rotary encoders. A laser tracker requires the use of a cooperative target such as an SMR. Laser trackers are designed to position its

laser beam always at the center of such retroreflectors. As the retroreflector moves, the trackers beam is steered using the tracker's internal motors until the forward and return beams coincide, resulting in the beam being maintained at the center of the retroreflector. The motion of an SMR can therefore be tracked in this manner. Measurement of a part or object by a laser tracker can thus be achieved by moving an SMR along the path to be measured, or positioning the SMR at the discrete points on the part to be measured and recording the measurements at the desired points. The corresponding points on the actual part can then be computed by compensating for the offsets accounting for the radius of the SMR as well as the offsets due to the nests used.

The organization of this thesis is as follows. Chapter 2 highlights the previous work in performance evaluation of laser trackers and describes how the present research has made contributions to this field. Chapter 3 goes on to describe the design and construction of the metrology bench. Chapter 4 brings out the measurement of error motions of the carriage along the rail of the bench. Chapter 5 demonstrates the use of the bench for ball bar calibration. Chapters 6 and 7 bring out two categories (back-to-back methods and common-path methods) of ranging test methods to evaluate the ranging capability of laser trackers, including modified approaches to each of these test categories. Chapter 8 concludes the thesis and briefly discusses future work.

CHAPTER 2: LITERATURE REVIEW

Several research efforts have been made to evaluate the performance of laser trackers. This section describes some of these efforts. The National Institute of Standards and Technology (NIST) developed a Laser Rail Calibration System (LARCS) which was deployed at NIST and at the Naval Surface Warfare Center (NSWC), Corona Division [1]. The LARCS was designed as a tool to enable positioning of a reference length in various configurations within the working volume of the tracker. This enabled exercising the angular encoders of the tracker to varying degrees, allowing the evaluation of the tracker's measurement capability for various configurations of the reference lengths. The system consisted of an optic rail supported at its ends by moveable tripods of adjustable height. This enabled the rail to be positioned in a variety of configurations. A reference laser interferometer was mounted on the rail by means of a mounting plate. A carriage that housed two nests, was mounted on the optic rail and positioned manually along the rail. This setup was used to perform a series of performance tests described in a draft standard dedicated to evaluating the performance of laser based instruments that use spherical coordinate systems, which was still under preparation then. A series of 99 length measurements and 108 two-face measurements were performed using a laser tracker with the LARCS system. The maximum error observed (tracker measured length minus reference interferometer displacement measurement) was 35 micrometers for a reference length of about 2.3 m created by the LARCS system. The expanded uncertainty (at the k=2

coverage level) for the LARCS-reported reference length was found to be 6.2 µm for the reference length of 2.3 m. Consequently, the tracker error/specification to LARCS uncertainty ratio was approximately 6:1, notably better than the commonly required 4:1 ratio.

Shortly thereafter, the ASME B89 committee on dimensional metrology approved the new U.S. national standard, ASME B89.4.19, Performance evaluation of laser-based spherical coordinate measurement systems [2]. This standard brought out two kinds of procedures for performance evaluation, namely system tests and ranging tests. Ranging tests described here were designed to evaluate the performance along a purely radial direction without using angle information. The standard recognized the use of a rail with a moving carriage monitored by a reference displacement interferometer as a possible method of evaluation of the performance of IFM as well as ADM systems. The system tests described in the standard involved measurement of calibrated reference lengths at a defined set of positions designed to be sensitive to known sources of laser tracker positioning errors. These tests were therefore analogous to volumetric performance tests for traditional Cartesian coordinate measuring machines (CMMs). The standard recognized the use of a rail-carriage system with an integral reference interferometer system as one of the possible ways to perform system tests as well. The standard also described two-face system tests, where targets were measured in front-sight and back-sight instrument orientations.

NIST describes their dedicated facility for performing the complete set of these B89.4.19 tests in [3]. This facility was used for testing the ranging capability of laser trackers. Their ranging test facility consisted of a 60 m laser rail and target carriage system.

A high accuracy wavelength corrected interferometer was used as a reference against which the performance of the laser tracker was compared. The carriage housed two retroreflector targets in a back-to-back configuration. The reference interferometer monitored one of these retroreflectors while the instrument under test (lase r tracker) monitored the other. The carriage was translated manually along the rail and the carriage displacement measured by the reference interferometer served as the reference length for each comparison against the instrument under test. Due to the large beam paths associated with such a setup, temperature was measured at seven locations along the rail, to allow for more effective environmental compensation. For a nominal reference length of L meters realized in their ranging test facility, the expanded uncertainty (at the k=2 coverage level) was observed to be U(L)= 5 µm + 0.4 x 10^{-6}L. Apart from laser trackers, their ranging test facility also allowed adaptation to test laser radars, time of flight scanners and other large scale optical measurement systems.

An alternative to this back-to-back method was put forward by NIST in [4], where a common air path is used for both the instrument under test as well as the reference laser. The setup consisted of accommodating the tracker's beam at the center of an SMR, while having the reference beam offset from the center. This allowed measurement using a single optic, which eliminated error sources due to offsets between front- and rear- facing optics used in the back-to-back method. A periscope was used to expand the separation between the forward and return reference beams in order to allow accommodation of a turning mirror within this space. The turning mirror served to reflect the tracker's beam along the rail towards the center of the retroreflector. Due to the increased separation between reference beams, a larger SMR of diameter 4 inch was used. The expanded uncertainty (at

k=2) for the realization of a nominal reference length L using this setup, was found to be U(L)=1.0 µm + 0.24 x 10^{-6} L, which was significantly lower than those realized for the back-to-back methods.

East Coast Metrology (ECM) presented a study [5] where a series of aluminum extrusions were used as the rails, and a three-meter reference length was measured over a range of distances. The setup of the rail system included three parallel rails of 10 m each, with a system of mirrors used in order to increase the range to 30 m. The observed expanded uncertainty (at k=2) was 3.37 µm for the 3 m reference length.

The work presented in the present research utilizes a design consisting of a framework similar to the frame used in [4] in that aluminum extrusions are used. Similar to the work described in [3], the rail-carriage system (metrology bench) was designed to perform ranging tests to evaluate the radial measurement capability of a laser tracker. Back-to-back ranging tests were carried out, but the traditional methods described in previous work was slightly modified to eliminate the influence of pitch and yaw of the carriage as it traveled along the rail. Further, an alternative approach to the common path method described in [4], is presented here, which eliminates some of the requirements of the setup presented by NIST. The setup proposed here does not require the accommodation of a mirror or a goniometer within the space between the forward and return reference beams. A periscoping system is also therefore not required to expand the spacing between reference beams to accommodating placement of optics. As a result of removal of this restriction, a smaller SMR can be used. Due to these reasons, it is believed that the proposed approach eases the setup process and also lowers cost.

CHAPTER 3: BENCH DESIGN AND CONSTRUCTION

3.1. MATERIAL CHOICE AND TESTING

Aluminum was chosen as the material primarily due to its light weight, machinability and consequent ease of availability and lower cost. Granite, although more desirable in terms of thermal stability, lower expansion coefficient and better vibration-dampening properties, would be very heavy and expensive, especially for a six-meter length that was desired for the bench. Consequently, extrusions of Aluminum 6105-T5 were obtained and tested using the cantilever test setup shown in Fig. 3.1.
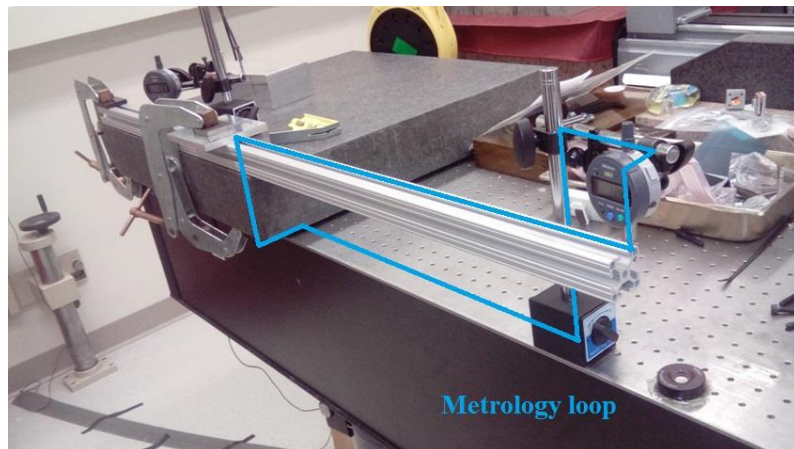
Fig. 3.1. Setup for determination of effective flexural rigidity

It was desired to minimize the size of the metrology loop used. Consequently, the beam was fixed parallel to the edge of the optic table using a granite slab. A slight overhang

of the granite slab from the table was necessary to provide room to hang weights. Such a setup allowed completion of the metrology loop through the optics table as opposed to the floor. The beam was fixed to the granite slab using two C-clamps. Metal blocks were used between the clamps and the beam to distribute the pressure and avoid distortion due to excess clamping force. A second indicator was used between the two C-clamps to ensure absence of bowing of the section between the two clamps when load is applied to the free end. This was done because such bowing could cause an apparent increase in deflection of the free end, which could by misattributed to the applied load. No bowing was observed.

The top surface of the free end of the beam when no load is applied does not represent the state of zero deflection, since this surface will already have deflected due to self-weight. However, this surface is still taken to be the datum for the measuring indicator, since the theory of superposition implies that the deflection due to self-weight is independent from the deflection due to an applied load. Fig. 3.2 shows the deflections observed in the beam for the various loads applied.
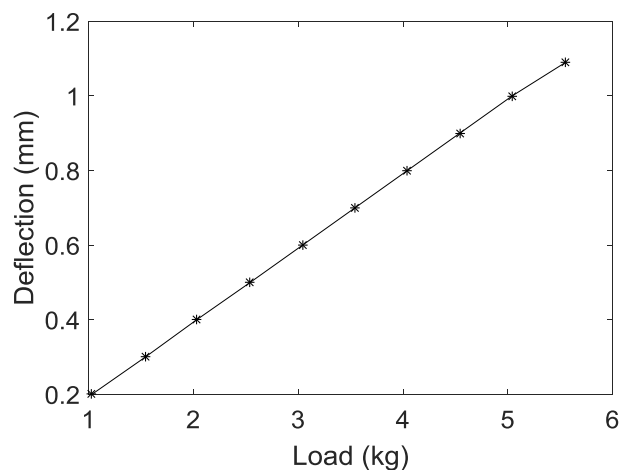
Fig. 3.2. Deflections observed in cantilever test

From the Load to deflection ratios observed, the effective flexural rigidity of the beam was calculated using equation 3.1.

$$EI = \left(\frac{W}{y}\right)\frac{L^3}{3} \tag{3.1}$$

Here, 'E' is the Young's modulus (in N/mm^2) and 'I' is the Moment of inertia (or second moment of area) of the beam (in mm^4) and therefore, 'EI' represents the flexural rigidity of the beam. 'L' is the length (in m) of the beam overhanging from the fixed end and 'y' is the deflection (in mm) corresponding to applied load 'W' (in N). The mean observed flexural rigidity was 3.761×10^9 N mm^2, as opposed to the value of 5.424×10^9 N mm^2 claimed by the manufacturer.

3.2. DESIGN

Fig. 3.3 (a) shows the cross section of the extrusion chosen for the main rail or guide rail that carried the carriage. Fig. 3.3 (b) shows the cross section of the extrusion chosen for the bench frame.
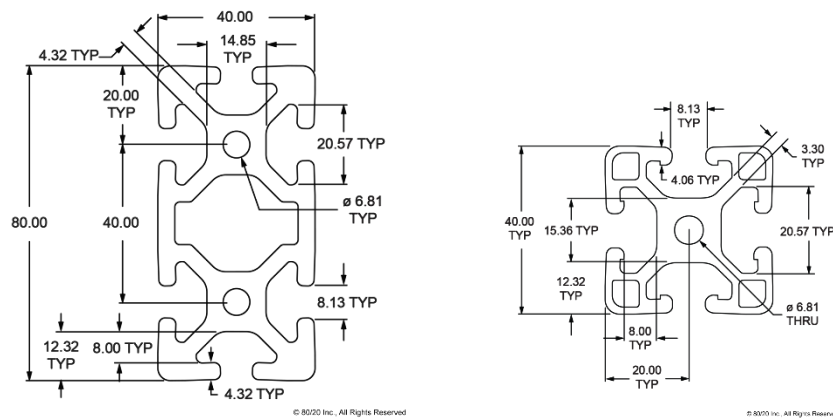
Image Courtesy: www.8020.net

Fig. 3.3. (a) Cross section of guide rail   (b) Cross section of frame

Based on the results of material testing, the maximum expected deflection due to self-weight (in an ideal case) was estimated to be 37.6 µm for a segment of the guide rail of length 1 m with a cross section shown in Fig. 3.3 (a) and fixed at both ends. Fig. 3.4 shows a CAD model of the bench frame and carriage system.

(a) Bench frame   (b) Carriage system
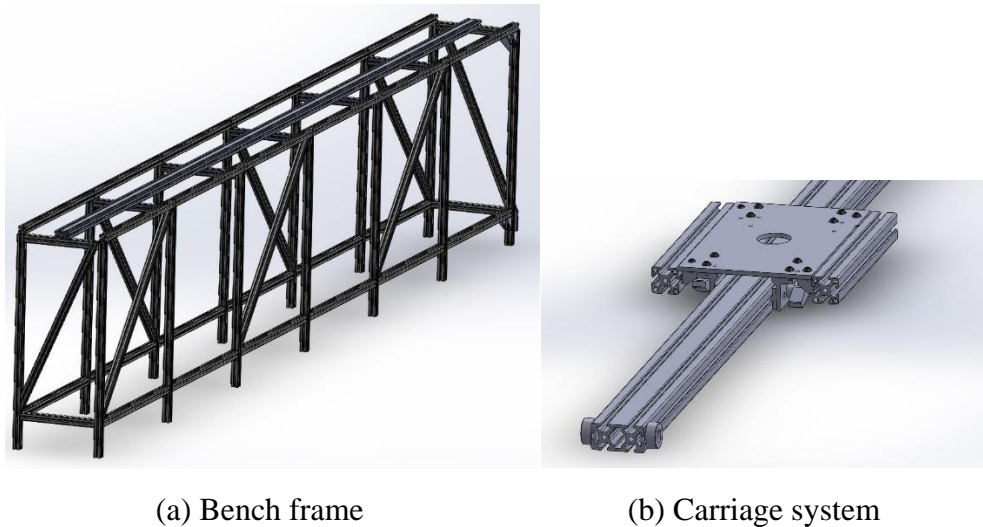
Fig. 3.4. CAD model of the metrology bench

It may be noted in the design that the diagonal support beams are located only in alternating segments of the bench frame. This was done for two purposes. Firstly, such a design reduced the material and therefore the cost. Secondly and more importantly, it was desired to have the horizontal beam/ rails at the joints (where one horizontal rail is fastened to another horizontal rail) fixed to the vertical supports on both sides to ensure maximum rigidity. Due to the nature of the pivots used to fasten the diagonal supports, these pivots could be fastened only to two members at the joint, of which one would be the diagonal member, and the other could be the horizontal beam or vertical support but not both. Having the diagonal supports in alternating segments allowed the horizontal beams to be

rigidly connected to the vertical supports on both sides at the joints where close alignment was critical.

3.3. CONSTRUCTION AND ALIGNMENT

The bench was constructed using aluminum extrusions obtained from 80/20 Inc. Fig.3.5 shows the constructed bench frame and carriage system.

(a) Bench frame   (b) Carriage system

Fig. 3.5. Constructed metrology bench

Following bench construction, the straightness of the guide rail was measured in two planes perpendicular to the longitudinal axis of the bench, namely the vertical plane (or z-straightness) and the horizontal plane (or y-straightness). These measurements were performed using a laser tracker which monitored a 0.5-inch-diameter SMR as it was moved manually along the rail. The measurement was a dynamic measurement where the tracker recorded points at every 50 mm of travel observed. Fig. 3.6 shows the setup of the SMR and pin nest used, and Fig. 3.7 depicts the right end of the guide rail, which shows the coordinate system used for reporting the straightness measurements.

Fig. 3.6. Setup for straightness
measurement

Fig. 3.7. Coordinate system for reporting
straightness measurement

The results of these initial straightness measurements are shown in Fig. 3.8. The short black lines shown on the graphical representation of the bench are to indicate that the guide rail was not a single beam of length 6 m, but rather three shorter rails of 2 m each. This explains the discontinuities observed at these locations.
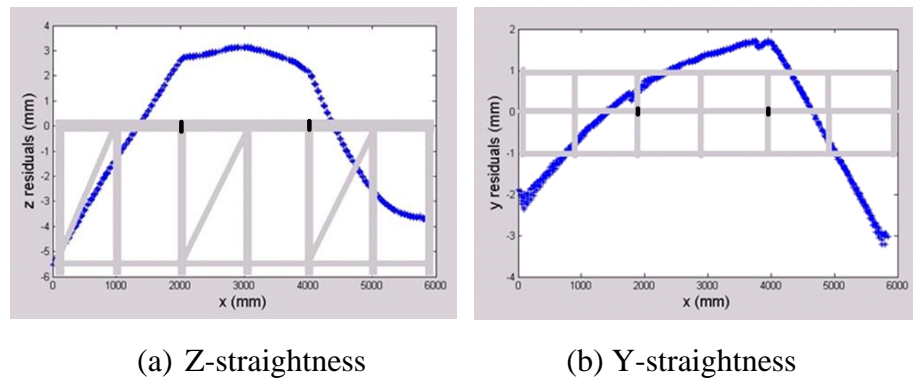
(a) Z-straightness

(b) Y-straightness

Fig. 3.8. Initial straightness errors of guide rail

These straightness parameters were found to be of the order of millimeters and were improved as described below. The Z-straightness was improved using leveling feet (shown

in Fig. 3.9) and Y-straightness was improved using fixtures that constrained the guide rail at the joints where one beam was connected to the next. This is shown in Fig. 3.10 (a). It was observed that this was not sufficient to maintain the straightness over long distances. Hence, two diagonal members were temporarily removed and used to constrain the straightness of the guide rail at these joints as shown in Fig. 3.10 (b). This was found to be effective in improving the straightness as desired.

Fig. 3.9. Adjustment of Z-straightness

(a)   (b)

Fig. 3.10. Adjustment of Y-straightness

After such alignments, straightness measurements were repeated using methods previously described. Fig. 3.11 shows the results of these post-alignment measurements.

(a) Z-straightness   (b) Y-straightness
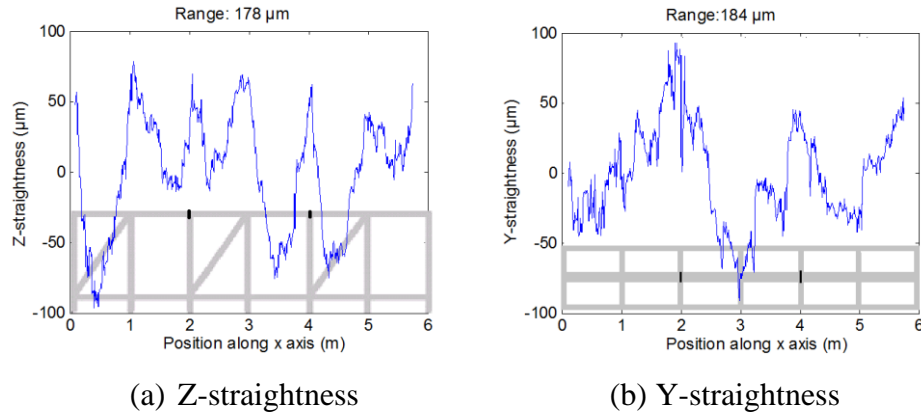
Fig. 3.11. Straightness errors of guide rail

Both straightness parameters could thus be constrained to within 200 µm.

3.4. ENVIRONMENTAL SENSORS

Due to large beam paths, temperature probes were mounted at seven locations along the bench at intervals of 1m. The probes were calibrated according to the methods described in the International Temperature Scale (ITS) of 1990 [6], or the ITS-90. This standard, however recommends the realization of ITS-90 fixed points using fixed point cells or melting point cells which are pieces of apparatus that are known for their ability to exercise rigorous control to maintain a uniform temperature (and often pressure). For probes expected to have an operation range of 0-29.7646 °C, the standard recommends calibration using only one temperature point (other than the triple point of water) fixed at 29.7646 °C, which corresponds to the melting point of gallium and can be realized by a gallium fixed point cell. Due to the absence of these equipment, the actual temperature points defined in the standard could not be used, and therefore, the probes were calibrated using a temperature point close to room temperature (25 °C) realized using a metrology well shown in Fig. 3.12. The coefficients for each probe were calculated according to the

procedures described in the standard. More information on the calibration methods used can be found in Appendix B.

Fig. 3.13 shows the deviations of these probes from the temperatures reported by the well when the well was set to 20˚C following probe calibration.

Fig. 3.12. Metrology well
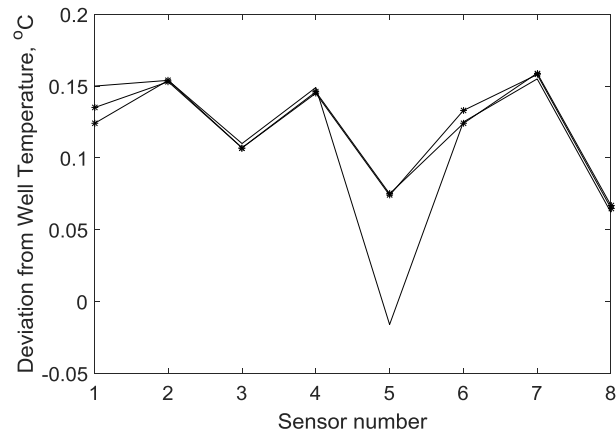
Fig. 3.13. Probe temperature deviations

It is clear from Fig. 3.13, that each temperature probe has a consistent bias. The bias for each probe is subtracted out before its recorded measurement data is used. Fig. 3.14 shows the mounting of these probes on the bench.

Fig. 3.14. Environmental sensor mounting

CHAPTER 4: MEASUREMENT OF ERROR MOTIONS OF CARRIAGE

It was desired to measure the error motions of the carriage as it traveled along the bench in order to obtain error maps for use in possible compensation procedures in other measurements performed using the rail-carriage system. This measurement of error motions of the carriage was also performed in order to characterize the stability of the bench or repeatability of the measured shape of the bench.

4.1. MEASURAND

The error motions measured the pitch, yaw, roll and the straightness along two axes mutually perpendicular to the longitudinal axis of the rail of the bench. The linear displacement error was not measured in this scenario since the positioning of the carriage along the bench was done manually.

4.2. MEASURING EQUIPMENT

The equipment used for measurement, was a six-degree-of-freedom laser interferometer from Automated Precision Inc. (API). This included the XD Laser head, a 5/6D sensor (or XD sensor), a reference level, a sensor probe capable of actively measuring air temperature and pressure, a material temperature sensor, and the X-D Laser Measuring system software. Fig. 4.1 shows the XD laser head and Fig. 4.2 shows the XD sensor, and Fig. 4.3 shows the GUI of the software.

Fig. 4.1. Laser Head
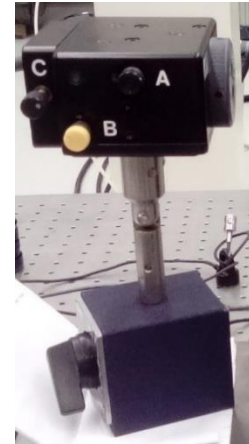
Fig. 4.2. XD sensor

Fig. 4.3. API Laser software GUI

4.3. EXPERIMENTAL SETUP

The API laser system that was used primarily consisted of a laser unit and a sensor unit. The laser unit included a laser head mounted on an adjustable base fixed to a magnetic base. The sensor unit included the XD sensor capable of measuring 5 of the 6 error motion parameters namely linear displacement accuracy, pitch, yaw, and two straightness parameters. Roll was measured by comparison to a reference level. The XD sensor was mounted onto a swiveling joint fixed to a magnetic base and mounted on the movable carriage. The laser unit was fixed on the end of the bench frame as shown in Fig. 4.4.
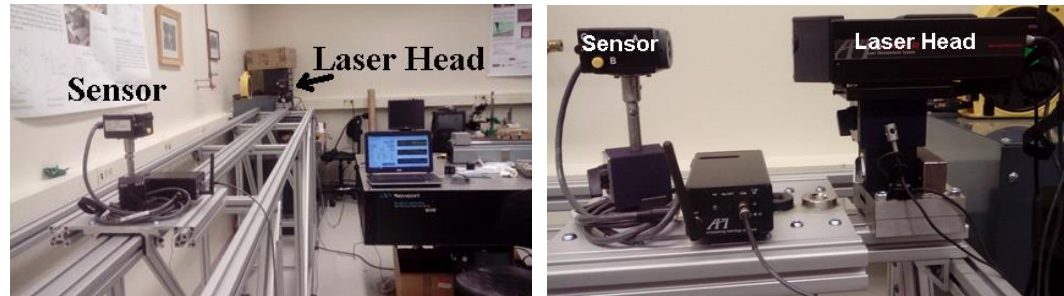
Fig. 4.4. Setup for measurement of error motions of carriage

A sensor probe included with the API laser was used for active measurement of air temperature and pressure. A material sensor was used for active measurement the temperature of the material. Fig. 4.5 shows the positioning of these sensors. Active humidity sensing could not be done due to absence of a humidity sensor. Hence, static humidity was assumed, the value for which was taken from the temperature recorded by the weather station of a Leica Laser Tracker system present in the laboratory, averaged over 30 minutes immediately prior to performing the measurement of the carriage.
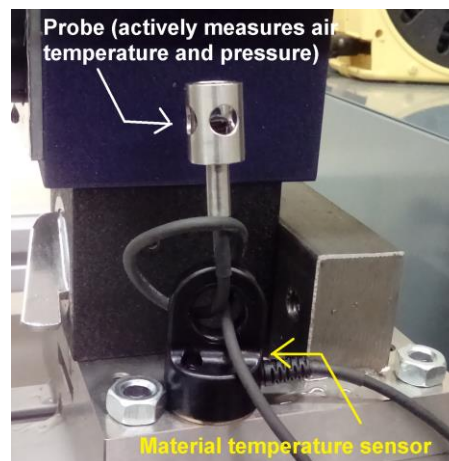
Fig. 4.5. Environmental sensors

Alignment of the laser beam along the line of travel of the carriage was performed according to the instructions provided in the XD Laser measurement system software. Due to the absence of machine axes along the vertical direction, translation of the laser head along this direction was achieved using steel blocks of appropriate height, while translation of the XD sensor in the vertical direction was achieved using step blocks. The dead path of the laser beam was approximately 150 mm.

4.4. MACHINE MODELING

A Frame based model was used to describe the system. Fig. 4.6 shows a block diagram of the machine configuration.
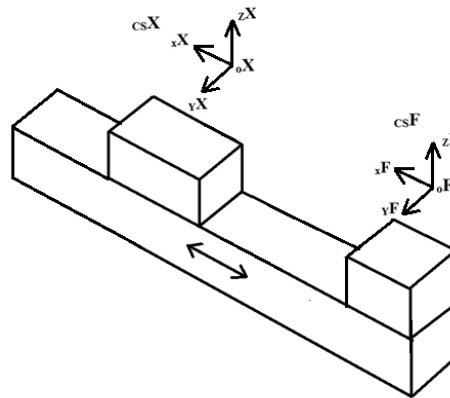
Fig. 4.6. Machine configuration

For the purposes of this model, the carriage shall henceforth be referred to as the 'table', while the remainder of the fixed structure of the bench shall be referred to as the 'frame'. The frame and table are assumed to be rigid bodies having their own coordinate systems denoted by the symbols csF and csX respectively. Table 4.1 shows the complete list of symbols used in this model.

Table 4.1. Notations used in error motion model

Symbol	Description
$_{cs}X$	Coordinate system of the table (X carriage)
$_{o}X$	Origin of $_{cs}X$
$_{x}X$	X axis of $_{cs}X$
$_{y}X$	Y axis of $_{cs}X$
$_{z}X$	Z axis of $_{cs}X$
$_{cs}F$	Coordinate system of the Frame
$_{o}F$	Origin of $_{cs}F$
$_{x}F$	X axis of $_{cs}F$
$_{y}F$	Y axis of $_{cs}F$
$_{z}F$	Z axis of $_{cs}F$
X_m	Departure of $_{o}X$ from home position along line of travel
$[X]_F$	Position vector of $_{o}X$ with respect to $_{cs}F$
$[T]_F$	Position vector of a point P on table with respect to $_{cs}F$
$[P]_X$	Position vector of point P with respect to $_{cs}X$
R_{XF}	Rotation vector for transformation from $_{cs}X$ to $_{cs}F$
δ_{XX}	Linear Displacement error along $_{x}F$ as X_m varies
δ_{YX}	Straightness error along $_{Y}F$ as X_m varies
δ_{ZX}	Straightness error along $_{z}F$ as X_m varies
ε_{XX}	Roll about $_{x}F$ as X_m varies
ε_{YX}	Pitch about $_{Y}F$ as X_m varies
ε_{ZX}	Yaw about $_{z}F$ as X_m varies

The origin ($_{o}X$) of the coordinate system of X ($_{cs}X$) is assumed to be along the normal to the table passing through the geometric center of the position sensing element within the XD sensor and at a height of approximately 162 mm from the table surface. $_{o}X$, and hence $_{cs}X$, moves with the carriage. The Z axis of $_{cs}X$ ($_{z}X$) passes though $_{o}X$ and is normal to the table surface. The direction of $_{z}X$ is taken to be positive along the direction in which the height from the table increases (vertically upward). The X axis of $_{cs}X$ ($_{x}X$) is assumed to be the average line that $_{o}X$ makes as X_m is varied. Positive direction of $_{x}X$ is taken to be along the direction that the carriage moves with respect to any stationary point

on the frame when X_m increases. The Y axis of csX ($_YX$) and its direction are defined by the cross product of $_zX$ and $_xX$ axis.

The right extreme position of the carriage along the rail is chosen as its home position. Fig. 4.7 shows a block diagram of the system when the carriage is in its home position. The coordinate system of the frame (csF) is assumed to be aligned with csX at the home position ($X_m=0$).
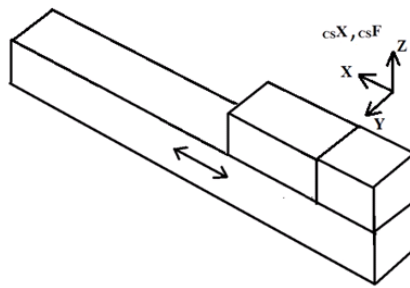
Fig. 4.7. Home position

As there is a table moving in only one axis (X axis), the nomenclature for a vector model of the system is XF. The vector model is briefly described by Fig. 4.8 and the equations that follow.
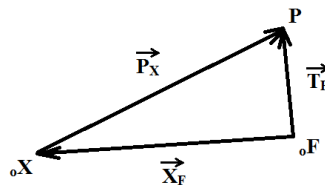
Fig. 4.8. Vector model

$$P_X + X_F = T_F \qquad (4.1)$$

$$[P]_X = R^{-1}{}_{XF} \{ [T]_F - [X]_F \} \tag{4.2}$$

Here,

$$[T]_F = \begin{bmatrix} t_X \\ t_Y \\ t_Z \end{bmatrix}_F \qquad [X]_F = \begin{bmatrix} -(X_m + \delta_{XX}) \\ \delta_{YX} \\ \delta_{ZX} \end{bmatrix}_F$$

$$R_{XF} = \begin{bmatrix} 1 & -\varepsilon_{ZX} & \varepsilon_{YX} \\ \varepsilon_{ZX} & 1 & -\varepsilon_{XX} \\ -\varepsilon_{YX} & \varepsilon_{XX} & 1 \end{bmatrix} \qquad R^{-1}{}_{XF} = R^T{}_{XF}$$

Fig. 4.9 shows the coordinate systems and the sign conventions used. Right hand rule was used for angular sign conventions. Sign conventions were checked by manually pushing on the XD sensor slightly. Signs that were found to be inverted, were corrected.
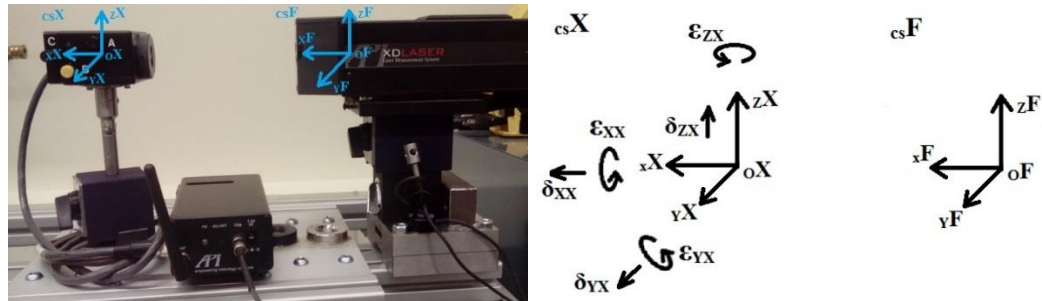
Fig. 4.9. Coordinate systems and sign conventions

4.5. MEASUREMENT METHODOLOGY

The five error motions of the carriage (δ_{YX}, δ_{ZX}, ε_{XX}, ε_{YX} and ε_{ZX}) were measured as the carriage was manually moved back and forth for 6 runs from 0 to about 5500 mm in steps of approximately 50 mm. The six runs were divided into two separate measurements performed on two different days, at different times of the day, in order to verify reproducibility, Day 1 included runs 1-2 and day 2 included runs 3-6.

4.6. RESULTS

Fig. 4.10 shows the error maps for the 5 error motion parameters measured. As seen from these error maps, there had been a datum shift between the two sets of measurement, but the overall shape of the bench was observed to be fairly repeatable.
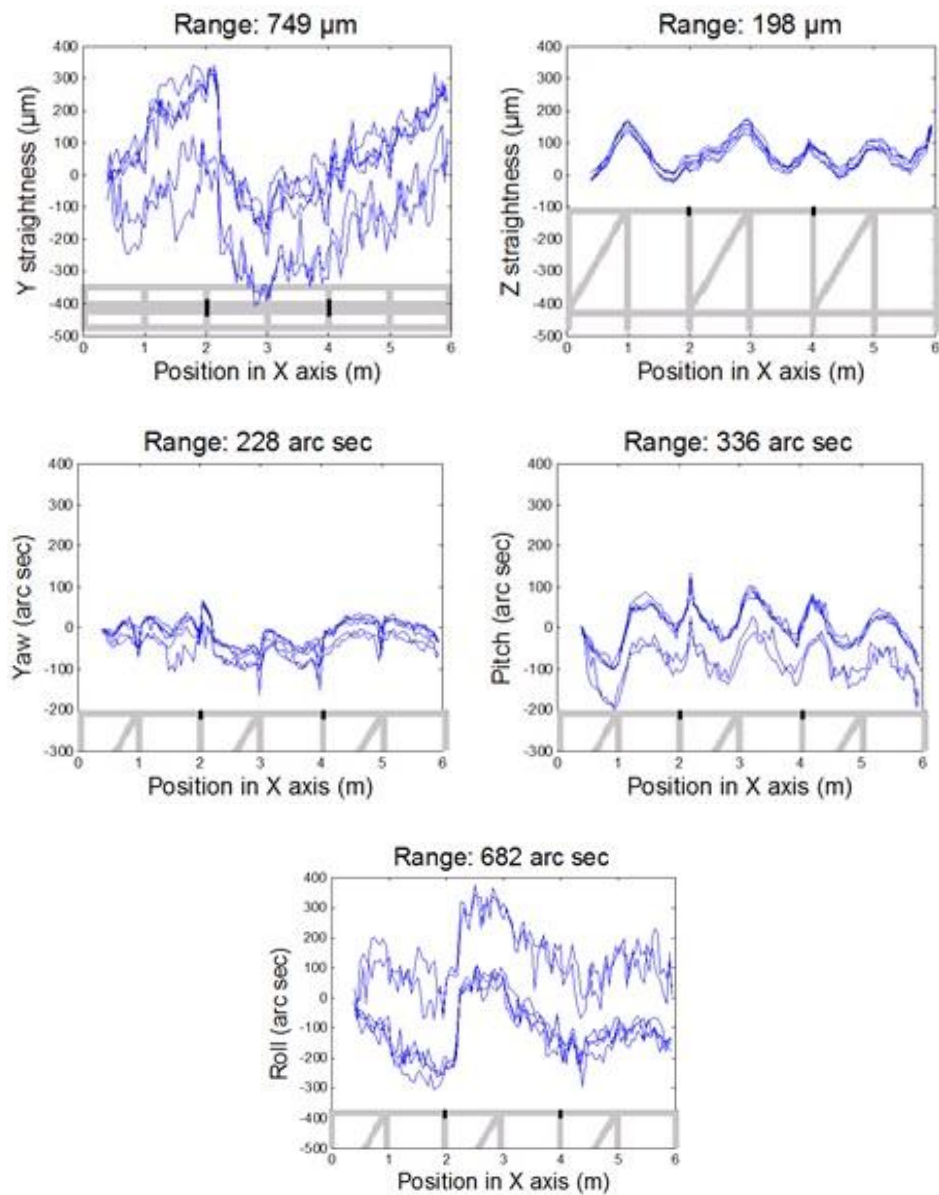
Fig. 4.10. Error maps

CHAPTER 5: BALL BAR CALIBRATION

Ball bar calibration is one of the applications that the constructed metrology bench was used for. Ball bars that have a seat at each end designed to hold an SMR, can be calibrated using the metrology bench and a laser tracker. This section describes the calibration procedures and results obtained.

5.1 MEASURAND

The measurand desired to be measured was the distance between the centers of SMRs mounted on either end of the ball bar at the temperature prevalent at the laboratory during the time of the measurement.

5.2. MEASURING EQUIPMENT

A Leica laser tracker of model AT901B (shown in Fig. 5.1) was used as the measuring instrument for the ball bar calibration. In order to use the laser tracker's ranging system to perform the calibration, this ranging system had to be independently calibrated by comparison with a traceable reference laser, thus allowing the results of ball-bar calibration to be traceable to established standards. Such comparisons of the tracker's ranging system to a reference interferometer are brought out in chapters that follow.

Fig. 5.1. Leica laser tracker

5.3. EXPERIMENTAL SETUP

The main objective of the set up was to align the beam of the laser tracker along the longitudinal axis of the bench, along which the ball bar length was to be measured. Such an alignment was desired in order to restrict the use of angular encoders which have relatively large uncertainties associated with the results of their angular measurements.

The steering mirror was fixed to a steel block which was in turn mounted using a magnetic base. This allowed the orientation of the steering mirror to be easily adjusted in the vertical and horizontal planes. This mounting of the mirror can be seen in Fig. 5.2, which also shows the positioning of the tracker's environmental sensors including air temperature probe and material temperature probe.
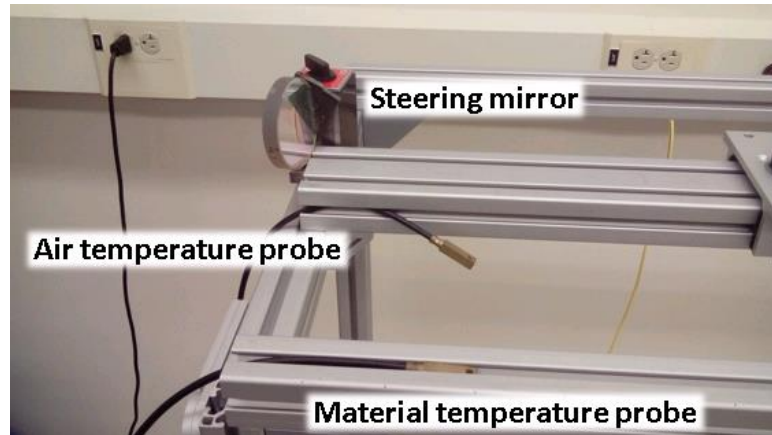
Fig. 5.2. Steering mirror and environmental sensors

The alignment of the tracker's beam along the bench was carried out using a steering mirror and a laser pointer mounted on a sphere of diameter 1.5 inch. The pointer was seated on a nest fixed to the bench. The beam from the pointer was then allowed to reach the steering mirror through a second sphere that a bore through its center, as shown in Fig. 5.3. The steering mirror was then adjusted to align the pointer's beam to enter the aperture of the tracker. This allowed the tracker to retrace the same path when its beam was directed at the steering mirror.

Fig. 5.3. Use of laser pointer for alignment of tracker's beam

Once the alignment is completed in this manner, the laser tracker will then view any pair of points on the guide rail of the bench as if they were in a straight line. This can be seen in Fig. 5.4, which shows the laser tracker's point of view.

Fig. 5.4. Tracker's point of view

5.4. MEASUREMENT METHODOLOGY

The measurement methodology involved measurement of each point over a period of one minute in order to obtain a point cloud from which the best estimate of that point is obtained. One nest was kept fixed while the other was left moveable. Fig. 5.5 briefly shows the methodology used. The first measurement involved positioning the SMR on the moveable nest and the sphere on the fixed nest. The beam reaching the SMR was then blocked and allowed to be reacquired using ADM. This was done to ensure that the IFM zero was set to the first point using ADM. It is to be noted that this zero cannot be set by IFM since the beam has to be reflected by the steering mirror, which implies that moving the SMR from the machine's internal homme position (bird bath) to the first point of

measurement cannot be done without having to break the beam at some point to allow reflection by the steering mirror.
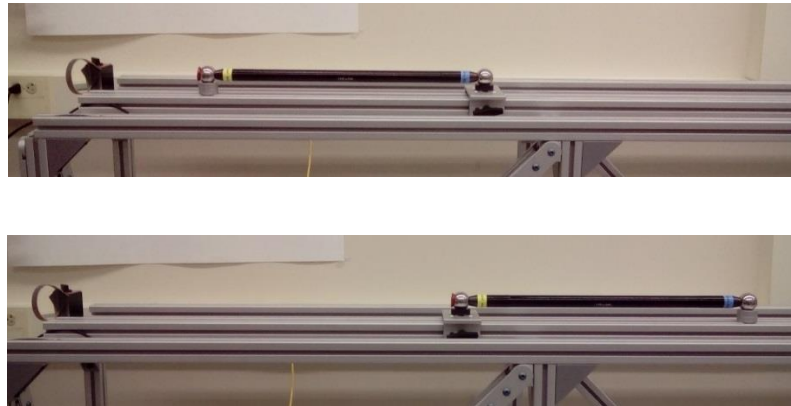
Fig. 5.5. Methodology for ball bar calibration

The first point was then measured over the desired time period to obtain a point cloud. The ball bar was then moved along the line of sight by a distance equal to the ball bar length. This was done by positioning the SMR on the fixed nest and the sphere on the moveable nest, after which the second point was measured. During such seating and unseating of the SMR, care is taken to avoid breaking of the beam.

It is to be noted that the fixed point can be established by locking the main carriage or one of the mini carts at a desired position along the bench. In this case, a mini cart was used as can be seen from Fig. 5.5. For such a case, the movable nest consisted of a stack of two nests. This was done to maintain the SMR at approximately the same height on the bench. When the main carriage is used to establish the fixed point, a stack of three nests is recommended to serve as the movable point. Such maintenance at the same height helps to restrict the use of the angular encoders. This is desired for reasons discussed in section 5.3.

The measurement methodology described in this section is repeated for three configurations of the ball bar. Fig. 5.6 shows these configurations.

Set 1 (Inline-near)   Set 2 (Inline-far)   Set 3 (Transverse)
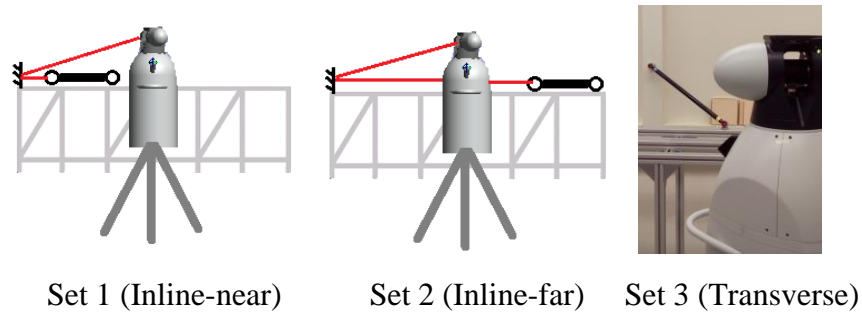
Fig. 5.6. Ball bar configurations used

The first configuration (set 1) involved a line-of-sight measurement where the ball bar was positioned close to the tracker. Set 2 was also a line-of-sight measurement but with the ball bar being positioned further away. The third configuration (set 3) was a transverse orientation of the ball bar chosen such that both angles varied by a significant amount between the two points.

Upon addition of temperature probes, further in-line measurements of the ball bar were performed at increasing distances from the steering mirror. For this second series of measurements, temperature compensation was applied as detailed in the following section.

5.5. MATHEMATICAL MODEL

The mathematical model used for the calibration of ball bars is shown in equation 5.1. This represents the distance between two points in spherical coordinate system and represents the model used for the propagation of uncertainties as described in the Guide to

the expression of uncertainty in measurement. The notations used in the model are shown

in Table 5.1.

<p style="text-align: center;">Table 5.1. Notations used in ball bar calibration model</p>

Symbol	Description
d	Measured distance between two points (m)
r_i	Range of point 'i' measured by tracker (m)
θ_i	Azimuth of point 'i' measured by tracker (rad)
$\emptyset_i$	Zenith of point 'i' measured by tracker (rad)
$d\theta_i, d\emptyset_i$	Change in azimuth and zenith of point 'i' from point 1 measured by tracker
K_t, K_p, K_h	Coefficient of refractive index change due to temperature, pressure and humidity respectively
T, T_p	Temperatures measured by tracker and relevant temperature probe respectively (°C)
ΔT	Change in temperature from probes (°C)
P	Pressure measured by tracker (mm Hg)
RH	Relative Humidity measured by tracker
V_p, V_{pn}	Vapor pressure of water corresponding to temperatures T and T_p respectively (mm Hg)

$$d = \sqrt{r_1{}^2 + r_2{}^2 - 2r_1r_2\left(\sin\emptyset_1 \sin\emptyset_2 \cos(\theta_1 - \theta_2) + \cos\emptyset_1 \cos\emptyset_2\right)} \qquad (5.1)$$

When temperature compensation was applied, the measurand d was estimated using a corrected range value r_{2c} given by equation 5.2.

$$r_{2c} = r_1 + 0.96 \times 10^{-6}\Delta T\, r_1 - (r_1 - r_2)C_T \qquad (5.2)$$

$$C_T = \frac{1 + K_t(T_p - 20) - K_p(P - 760) + K_h(V_{pn} * RH - 10)}{1 + K_t(T - 20) - K_p(P - 760) + K_h(V_p * RH - 10)}$$

$$d = \sqrt{r_1{}^2 + r_{2c}{}^2 - 2r_1 r_{2c}[\sin\phi_1 \sin\phi_2 \cos(\theta_1 - \theta_2) + \cos\phi_1 \cos\phi_2]}$$

5.6. RESULTS AND DISCUSSION

The estimates of the length of the ball bar and the uncertainties associated with these estimates are brought out in Fig. 5.7. These results correspond to instrument self-compensation, where the individual temperature probes on the bench were not used. The triangles pointing up and down represent the error bars corresponding to the k=2 expanded uncertainties.
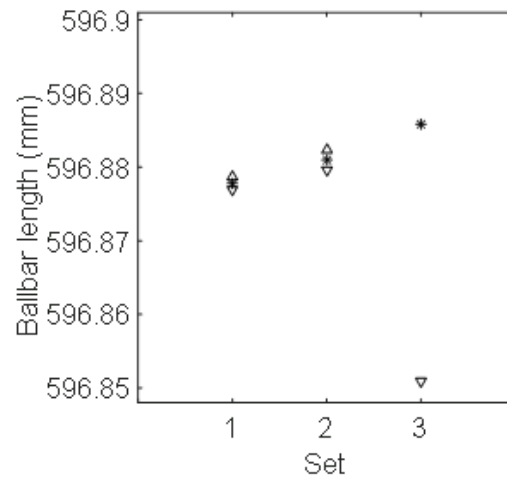
Fig. 5.7. Results of ball bar calibration (no compensation)

From the results, it can be observed that the transverse configuration shows a significantly higher uncertainty associated with the measurement result. This can be attributed to the large variation in angles and serves as a demonstration as to why line-of-

sight measurement is preferred. Table 5.2 shows the uncertainty contributions from various sources for the three configurations of the ball bar. Detailed uncertainty budgets for all measurements can be found in Appendix A.

Table 5.2. Uncertainty contributions for ball bar calibration

Contributor	Uncertainty contribution (µm)		
	Inline-near	Inline-far	Transverse
Range- 1st/near point	0.23	0.48	0.07
Range- 2nd/far point	0.34	0.49	0.07
Azimuth- 1st/near point	0.08	0.08	9.12
Azimuth- 2nd/far point	0.08	0.08	9.12
Zenith- 1st/near point	0.02	0.00	8.50
Zenith- 2nd/far point	0.02	0.00	8.16

From Table 5.2, it is clear that the uncertainties due to the angular encoders are the dominating contributors toward the large uncertainty associated with the transverse case. It is to be noted that measurement performed for this transverse case is only to demonstrate the larger uncertainty resulting from the increased variation of angles. This measurement does not represent a case of ball bar calibration. The calibration cases include only the in-line measurements. With the exception of the measurement of the ball-bar in this transverse case, all the remaining measurements described in this thesis involve use of a steering mirror to reflect the tracker's beam. For all such measurements, the uncertainty due to the non-flatness and curvature of the mirror is assumed to be of the order of nanometers or

lower (assuming the first surface of the mirror to be flat to less than λ/4 at 633 nm) and therefore neglected.

Fig. 5.8 shows the results of the ball bar measurements that were performed following the installation of the individual temperature probes on the bench. These measurements were taken at increasing distances from the steering mirror. The numbers above the error bars on the figure indicate the differences (in µm) from the tracker's self-compensated values. For example, for the measurement performed at approximately 3 m from the mirror, when the individual temperature probes were used for thermal compensation, the tracker measured the ball bar to be 0.52 µm shorter than when only the instrument's self-compensation was used for the same measurement.
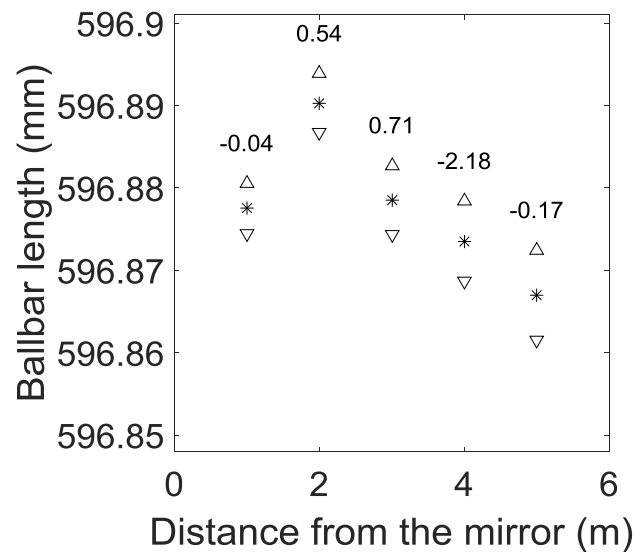
Fig. 5.8. Results of ball bar calibration (with compensation)

The uncertainties shown as error bars in Fig.5.8 represent the k=2 expanded uncertainties. Table 5.3 shows the sources of uncertainty considered, and their

contributions for one of the measurement cases. Detailed uncertainty budgets for all measurements can be found in Appendix A.

Table 5.3. Uncertainty contributions- ball bar calibration with compensation

Uncertainty source	Contribution (µm)	Uncertainty source		Contribution (µm)
Range- point 1	0.07	Vapor pressure of water		0.00
Range- point 2	0.08	Temperature from probe		0.28
Azimuth- point 1	0.00	Change in temperature (probe)		1.77
Azimuth- point 2	0.02	Vapor pressure of water corresponding to temperature from probe		0.01
Zenith- point 1	0.00			
Zenith- point 2	0.05			
Temperature	0.00	Coefficient of refractive index change due to	Temperature	0.00
Pressure	0.00		Pressure	0.00
Relative Humidity	0.00		Humidity	0.00

CHAPTER 6: BACK TO BACK RANGING TESTS

A ranging test involves evaluation of the ranging capability of instruments such as laser trackers by comparison against stable reference laser interferometers. The performance of IFM or ADM of a laser tracker can be tested using this test. A back to back test is a ranging test method for a laser tracker, wherein two SMRs are mounted on a carriage in a back-to-back fashion and each SMR is monitored by the instrument it faces (laser tracker or reference laser).

6.1. MEASURAND

The carriage that houses two back-to-back SMRs is moved along the guide rail of the bench. The distance moved by the carriage is measured by the laser tracker as well as the reference laser. The reference laser performs a pure interferometric measurement while the tracker measures the distance using interferometry as well as angular encoders. The measurand is the carriage displacement measured by the tracker minus that measured by the reference interferometer.

6.2. MEASURING EQUIPMENT

The measuring instrument used was a Leica laser tracker of model AT901B. The tracker's ranging performance was evaluated by comparison with a HP 5228A Laser measurement system, which was used as the reference laser interferometer. Fig. 6.1 shows

the reference laser and its controller.

Fig. 6.1. Reference laser and controller

6.3. EXPERIMENTAL SETUP

The setup for the back to back test primarily involved alignment of the reference laser's beam and the laser tracker's beam along the bench but in opposite directions such that each beam reached one of two SMRs mounted back-to-back on the carriage. A block diagram of such a setup is shown in Fig. 6.2, which also brings out the measurand definition.
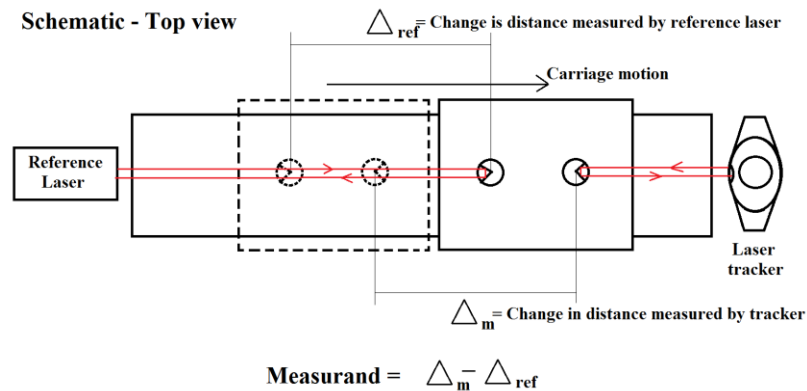
Fig. 6.2. Block diagram of setup for back to back ranging test

The tracker can be lowered in height till its beam is parallel to the beam of the reference laser as shown in Fig.6.2. The tracker would then be said to be bucked in. Since such bucking in was not very practical due to lack of room, the setup was achieved using a steering mirror as shown in Fig. 6.3. The tracker's beam was aligned along the bench using a laser pointer as mentioned in section 5.3.
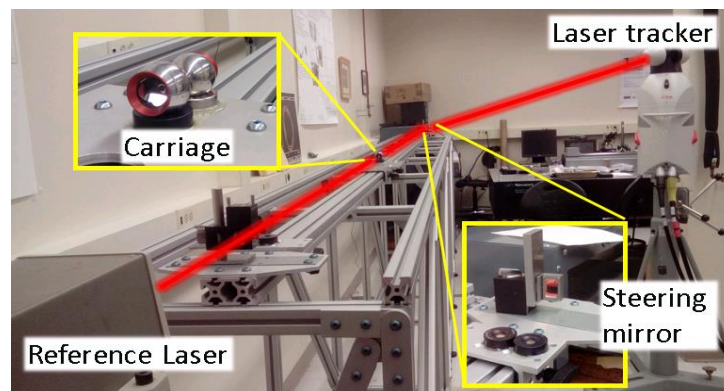
Fig. 6.3. Setup for back to back ranging test

The reference laser was aligned along the bench using an SMR mounted on the carriage. The laser head was translated when the carriage was at the closest position and rotated when the carriage was at the farthest position, such that the return beam always reached the approximate center of a target over the return aperture of the laser head at all positions of the carriage. The beam splitter and reference interferometer were mounted on a mounting platform fastened to the guide rail of the bench.

6.4. MEASUREMENT METHODOLOGY- FOUR POINT METHOD

Two methodologies are presented for the back to back ranging test, namely a four-point method and a two-point method. Both these methods are slightly different from the

conventional back-to-back method described in [1]. This section describes the methodology for the four-point method.

Due to the nature of the back-to-back setup, the position of the two SMRs relative to the laser interferometer measurement path varies as the carriage moves. This variation is due to the pitch and yaw error motions of the carriage and results in an Abbe error. In the work described in [1], the pitch and yaw of the carriage along the rail was measured using angular optics and thus accounted for. The present work also involved measurement of pitch and yaw along with other error motions as described in chapter 4. However, it was recognized that using the results of these measurements would introduce additional sources of uncertainty, since the position of the sensing element within the sensor head was not accurately known. Similarly, the positioning of the laser source within the laser head was not accurately known. Additionally, the reference coordinate systems were different for the error motion measurement and back to back test. Further, the yaw and pitch at a particular point is expected to change over time due to day-to-day use of the bench which could cause relative motion between structural elements.

It was desired to reduce the sources of uncertainty and therefore, the conventional methodology was modified such that the pitch and yaw information can be obtained from the same setup. The conventional methodology involves only step 2 and 3 shown in Fig. 6.4 (c) and (d), where the carriage moves and each instrument monitors the corresponding SMR. The methodology presented here adds an additional step, which is the measurement of the reference nest by the tracker. This was done before and after carriage motion as shown in Fig. 6.4.

Such measurement of the tracker nest by the laser tracker was used to identify the initial orientation of the vector pointing from the reference nest to the tracker nest. After motion of the carriage, the final orientation of this vector was observed. This allowed the realization of the combined effect of pitch and yaw of the cart as it moved along the rail. This information was then used to account for the error introduced due to pitch and yaw of the cart, as explained in section 6.5.

(a) Schematic showing layout and location of points measured

(b) Measurement of point 1 by laser tracker

(c) Measurement of point 2 by laser tracker and setting of point 1 as zero point for reference interferometer

(d) Measurement of point 3 by laser tracker and carriage displacement by reference interferometer

(e) Measurement of point 4 by laser tracker
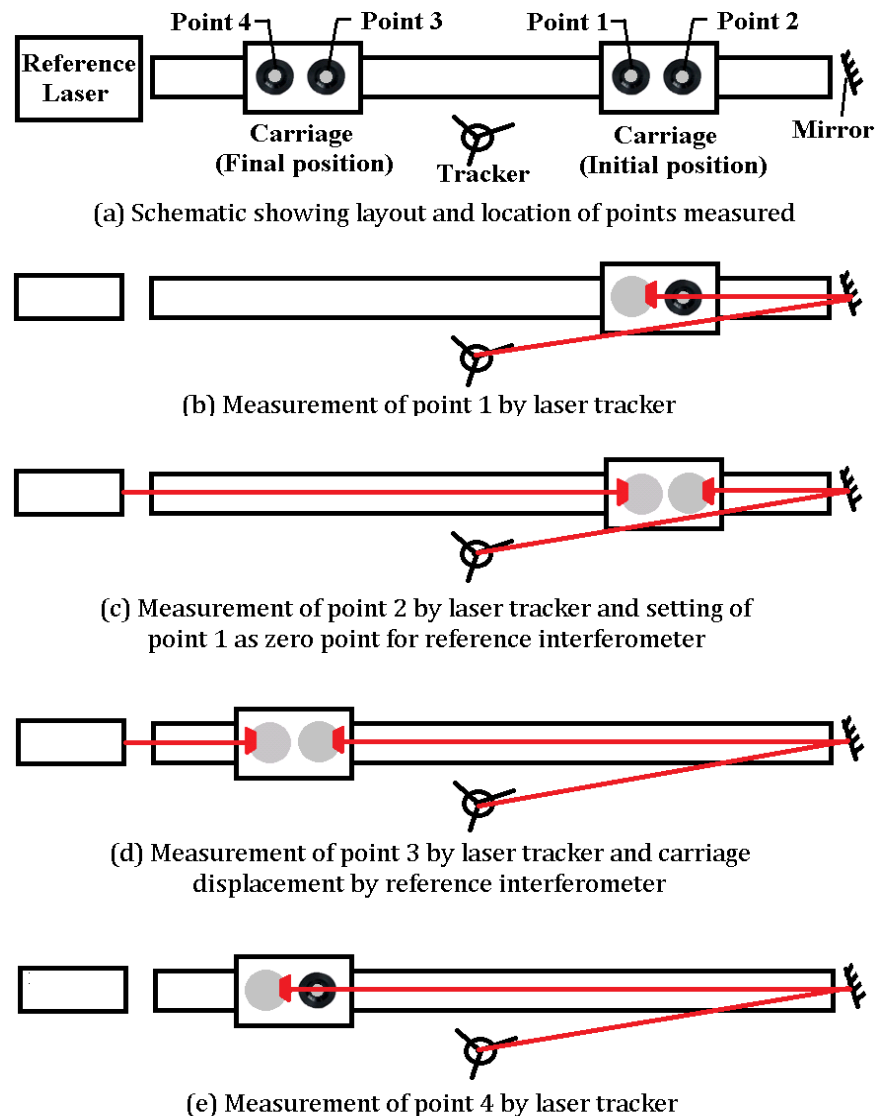
Fig. 6.4. Measurement methodology for four point method

This methodology was then repeated for various measurement times. This was done to observe the influence of measurement time on the measurand and the uncertainty in its estimate.

6.5. MATHEMATICAL MODEL- FOUR POINT METHOD

The objective of the model presented here, was to capture the influence of as many contributors as possible. Table 6.1 shows the terms used in the model.

Table 6.1. Notations used in back to back model- four point method

Notation	Description
d	Measurand (ranging error)
$r_i, \theta_i, \emptyset_i$	Range, Azimuth and Zenith of point 'i' measured by tracker
$d\theta_i, d\emptyset_i$	Change in azimuth and zenith of point 'i' from point 1 measured by tracker
x_i, y_i, z_i	Points in Cartesian coordinates
α_1	Acute angle made by $\overrightarrow{b_1}$ with $\overrightarrow{b_2}$
α_2	Acute angle made by $\overrightarrow{b_3}$ with $\overrightarrow{b_2}$
ε	Error due to combined effect of pitch and yaw
R	Displacement measured by reference interferometer
C	Atmospheric correction factor for reference interferometer
T, P, RH, Vp	Atmospheric conditions (Temperature, Pressure, Relative Humidity, Vapor pressure of water respectively)
K_t, K_p, K_h	Coefficient of refractive index change due to temperature, pressure and humidity respectively

Fig. 6.5 is a graphic representing how the combined influence of pitch and yaw is captured in the model. At the time these measurements were performed, temperature sensors on the bench were not installed, and the reference laser did not have an environmental compensation module. Environmental correction was therefore performed for the reference laser using the values from the environmental sensors of the tracker system. Only instrument self-compensation was used for the tracker for the four point method.
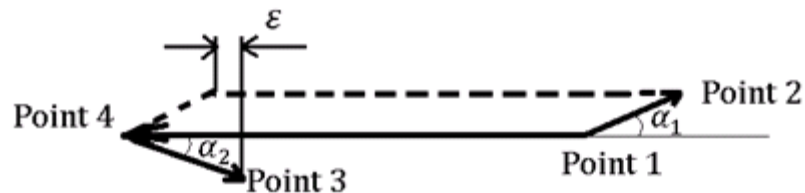
Fig.6.5. Error due to pitch and yaw

$$x_i = r_i \sin \emptyset_i \cos \theta_i$$

$$y_i = r_i \sin \emptyset_i \sin \theta_i$$

$$z_i = r_i \cos \emptyset_i$$

$$\vec{b_1} = \begin{bmatrix} x_4 - x_1 \\ y_4 - y_1 \\ z_4 - z_1 \end{bmatrix} \; ; \; \vec{b_2} = \begin{bmatrix} x_2 - x_1 \\ y_2 - y_1 \\ z_2 - z_1 \end{bmatrix} \; ; \; \vec{b_3} = \begin{bmatrix} x_3 - x_4 \\ y_3 - y_4 \\ z_3 - z_4 \end{bmatrix}$$

$$\cos \alpha_1 = \frac{\vec{b_1} \cdot \vec{b_2}}{|\vec{b_1}||\vec{b_2}|} \quad ; \quad \cos \alpha_2 = \frac{\vec{b_1} \cdot \vec{b_3}}{|\vec{b_1}||\vec{b_3}|}$$

$$\varepsilon = \frac{|\vec{b_2}| + |\vec{b_3}|}{2}(\cos \alpha_1 - \cos \alpha_2)$$

$$d = \sqrt{r_1{}^2 + r_2{}^2 - 2r_1 r_2 [\sin \phi_1 \sin \phi_2 \cos(\theta_1 - \theta_2) + \cos \phi_1 \cos \phi_2] + \varepsilon - R.C}$$

$$where\ C = 1 + K_t(T - 20) - K_p(P - 760) + K_h(V_p * RH - 10)$$

6.6. RESULTS AND DISCUSSION- FOUR POINT METHOD

Fig. 6.6 shows the results obtained for this measurement. From the figure, no apparent trend of the uncertainty as a function of measurement time is observed. However, the estimate of the error appears to increase with increasing measurement time. This is likely due to the fact that the temperature variation is larger for a larger time period of measurement. The range of temperature variation was found to be 0.1˚C for the first case (shortest measurement time) and 0.4˚C for the last case (largest measurement time).
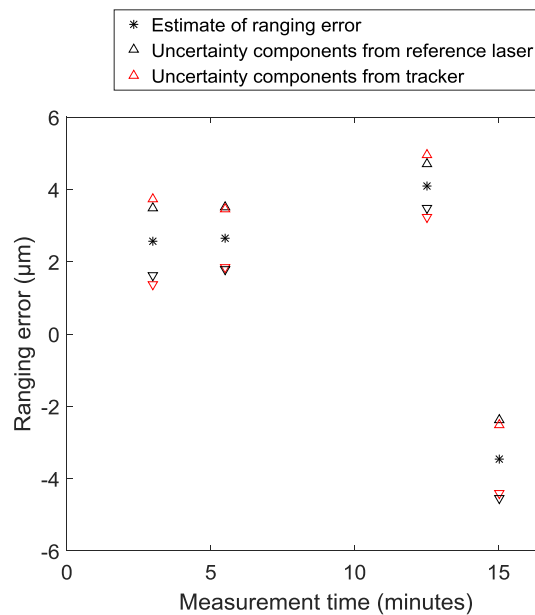
Fig. 6.6. Results- Four point method

Table 6.2 shows the uncertainty sources accounted for, and their contributions for one of these measurements. Detailed uncertainty budgets for all measurements can be found in Appendix A.

Table 6.2. Uncertainty contributors- four point method

Contributor	Uncertainty contribution (µm)	Contributor		Uncertainty contribution (µm)
Range- point 1	0.00	Zenith- point 3		0.16
Range- point 2	0.11	Zenith- point 4		0.21
Range- point 3	0.22	Reference laser reading		0.21
Range- point 4	0.00	Temperature		0.38
Azimuth- point 1	0.00	Pressure		0.02
Azimuth- point 2	0.02	Relative humidity		0.02
Azimuth- point 3	0.03	Vapor pressure of water		0.01
Azimuth- point 4	0.02	Coefficient of refractive index change due to	Temperature	0.00
Zenith- point 1	0.00		Pressure	0.00
Zenith- point 2	0.19		Humidity	0.00

6.7. MEASUREMENT METHODOLOGY- TWO POINT METHOD

This section describes a two point method, where the influence of pitch and yaw of the cart are eliminated. The sequence of steps is the same as that described in Fig. 6.4. However, since the tracker measures the position of the reference nest before and after carriage motion (points 1 and 4), it was realized that the tracker did not need to measure the tracker nest at all. This resulted in both instruments measuring the same points (points 1 and 4) and therefore eliminated the problem of variation of the offsets between the two SMRs with carriage motion.

6.8. MATHEMATICAL MODEL- TWO POINT METHOD

This model involves thermal compensation for the reference laser as well as the tracker using the individual probes mounted on the bench. Further, this model also uses this thermal information to account for dead path errors, as these errors can be appreciable over the several meters of dead path encountered by the tracker due to the nature of a back-to-back configuration. Table 6.3 shows the notations used in this model.

Table 6.3. Notations used in back-to-back model- two point method

Symbol	Description
d	Measurand (Ranging error)
$r_i, \theta_i, \emptyset_i$	Range, Azimuth and Zenith of point 'i' measured by tracker
$d\theta_i, d\emptyset_i$	Change in azimuth and zenith of point 'i' from point 1 measured by tracker
r_{4c}	Corrected value of r_4 from tracker
R	Carriage displacement measured by reference laser
ΔT	Change in temperature during measurement
K_t, K_p, K_h	Coefficient of refractive index change due to temperature, pressure and humidity respectively
T, T_p, T_R	Temperatures measured by tracker, relevant probes and reference laser respectively
P, P_R	Pressure measured by tracker and reference laser respectively
RH	Relative Humidity measured by tracker
V_p, V_{pn}, V_{pr}	Vapor pressure of water corresponding to temperatures T, T_p and T_r respectively
C_T, C_R	Correction factor for tracker and reference laser respectively

$$r_{4c} = r_1 + 0.96 \text{ x} 10^{-6} \varDelta T \, r_1 - (r_1 - r_4) C_T$$

$$C_T = \frac{1 + K_t (T_p - 20) - K_p (P - 760) + K_h (V_{pn} * RH - 10)}{1 + K_t (T - 20) - K_p (P - 760) + K_h (V_p * RH - 10)}$$

$$d = \sqrt{r_1^2 + r_{4c}^2 - 2r_1 r_{4c} [\sin \phi_1 \sin \phi_4 \cos(\theta_1 - \theta_4) + \cos \phi_1 \cos \phi_4]} - R.C_R$$

$$C_R = \frac{1 + K_t (T_p - 20) - K_p (P - 760) + K_h (V_{pn} * RH - 10)}{1 + K_t (T_r - 20) - K_p (P_r - 760) + K_h (V_{pr} * 0.5 - 10)}$$

6.9. RESULTS AND DISCUSSION- TWO POINT METHOD

Fig. 6.7 shows the results of ranging tests using the two point method. These measurements were taken for increasing values of carriage displacements. The numbers above the error bars on the figure indicate the improvement (in µm) that resulted from environmental compensation (including dead path correction) of the tracker as well as reference laser using temperature information from individual probes as opposed to using instrument self-compensated values. For example, for the measurement performed for approximately 2.5 m of carriage motion, when the individual temperature probes were used for thermal compensation, the ranging error of the tracker improved by 14.3 µm (increased from -12.7 µm to 1.6 µm) compared to when the tracker and reference laser used only self-compensation for the same measurement.

Table 6.4 shows the sources of uncertainty considered, and their contributions for one of the measurement cases. The contributions have the same trend for all the cases. Detailed budgets for all cases are found in Appendix A.
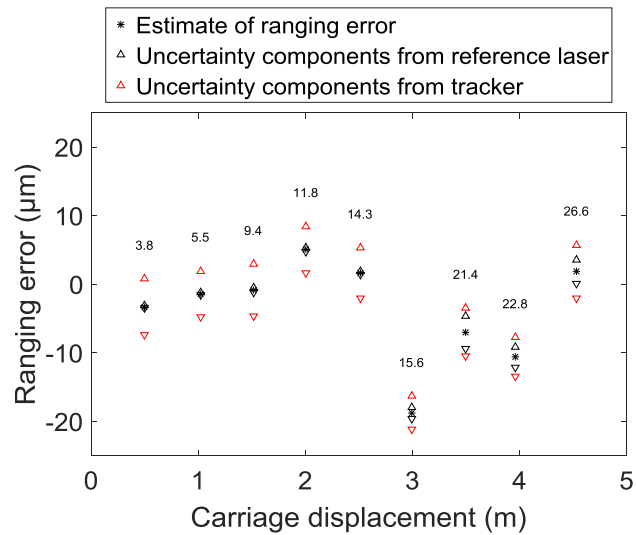
Fig. 6.7. Results- Two point method

Table 6.4. Uncertainty contributions- Two point method

Uncertainty source	Contribution (µm)	Uncertainty source		Contribution (µm)
Range- point 1	0.46	Temperature (reference laser)		0.07
Range- point 2	0.77	Pressure (reference laser)		0.17
Azimuth- point 1	0.00	Temperature (probes)		0.10
Azimuth- point 2	0.76	Change in temperature (probes)		3.22
Zenith- point 1	0.08	Vapor pressure of water corresponding to temperature from	Tracker	0.00
Zenith- point 2	0.03		Probes	0.00
Reference laser reading	0.38		Reference laser	0.00
Temperature (tracker)	0.06	Coefficient of refractive index change due to	Temperature	0.00
Pressure (tracker)	0.17		Pressure	0.00
Relative Humidity (tracker)	0.15		Humidity	0.00

CHAPTER 7: COMMON PATH METHOD

Unlike the back-to-back ranging test methods described in Chapter 6, a common path method utilizes a common air path for the reference laser and the laser tracker under test. This means that the test can be performed using a single optic shared by the two instruments. Such a common path method takes advantage of the fact that a laser tracker's beam is maintained at the center of an SMR, while the beams of a reference laser do not need to. This allows a single optic to be used as long as the beams can be accommodated in this way.

7.1. MEASURAND

As a carriage with an SMR mounted on it was allowed to move, and its displacement was monitored simultaneously by a tracker and a reference laser. The measurand was the deviation of the tracker-measured carriage displacement from the corresponding reference length given by the same displacement measured by the reference interferometer.

7.2. MEASURING EQUIPMENT

A Leica AT901B model laser tracker was the instrument under test. A HP 5228A Laser measurement system was used as the reference laser. Additionally, a steering mirror was used, but no periscope or a large SMR was used.

7.3. EXPERIMENTAL SETUP

The setup for a common path method presented by NIST in [4] lists three essential requirements for the setup. First, it required a periscoping system to expand the distance of separation between the forward and return beams of the reference laser. Such increase in separation was required in order to accommodate a tuning mirror within that space. Secondly, this mirror needed to be small enough and mounted on a goniometer that also needed to be small enough to fit in the space between the reference beams. Third, a large retroreflector was needed to accommodate the beams due to the increased separation between them. The setup proposed in the present research however, eliminates all three of these requirements for a common-path setup. Although a steering mirror/ turning mirror was used in the proposed setup, it was not mandatory to be used. Bucking the tracker in would allow the tracker's beam to enter in the required direction and therefore a mirror would not be required. Fig. 7.1 shows a schematic of the NIST setup (or the periscope method) and Fig 7.2 shows a schematic of the proposed setup (or the beam splitter method) where the task of accommodation of the beams in a common air path to a shared SMR, is accomplished by the beam splitter of the interferometer.
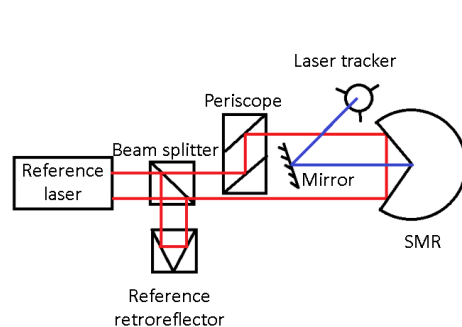
Fig. 7.1. NIST setup
(Periscope method)
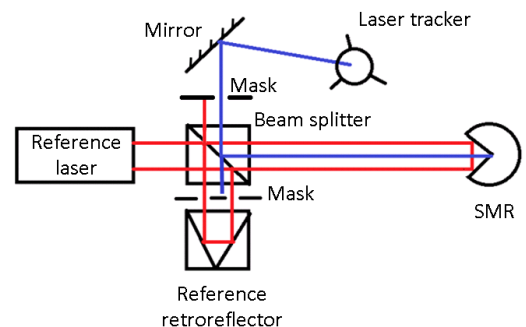
Fig. 7.2. Proposed setup
(Beam-splitter method)

The mask depicted in Fig. 7.2 (photographed in Fig 7.3) fits around the beam splitter and serves two important functions. First, it prevents the tracker's beam from entering the reference retroreflector and therefore prevents it from being tracked instead of the SMR. Second, it prevents the reference laser beam from entering the tracker's aperture via reflection by steering mirror.
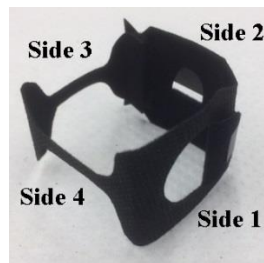
Fig. 7.3. Mask for beam splitter method

This section describes a simplified alignment procedure using the mask shown in Fig. 7.3. The orientation of the mask fitted around the beam splitter is such that the side 1 faces the target SMR on the carriage. Sides 2, 3 and 4 therefore face the mirror, reference laser and reference retroreflector respectively. The mask is first adjusted in the vertical direction until the reference laser is able to monitor an SMR on the carriage. This ensures that the reference laser beams are not blocked by the strip on side 3 of the mask. A laser pointer is directed towards side 1 such that it reaches the center of the strip on side 3. This will mean that the beam also reaches the center of the strip on side 4 and therefore blocked from reaching the reference retroreflector. The beam from the pointer then leaves the mask through side 2. The mirror is then adjusted till this pointer beam enters the tracker aperture. This allows the tracker to retrace the same path as the pointer. Side 2 of the mask blocks

the reference laser beam from reaching the mirror and therefore prevents it from entering the tracker aperture. Between the mirror and side 2 of the mask, a polarization rotator (such as a half wave plate) may be necessary to ensure that the tracker beam enters and exits the beam splitter with the correct polarization. Fig. 7.4 shows the setup for the beam splitter method.
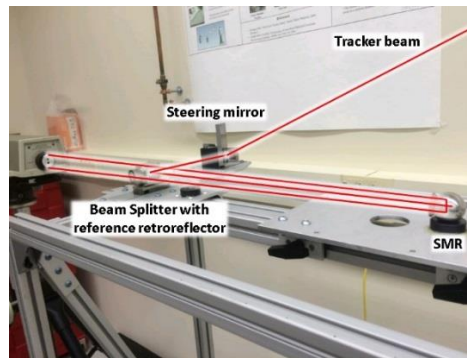
Fig. 7.4. Setup for common path test- beam splitter method

7.4. MEAUREMENT METHODOLOGY

The measurement methodology involved simultaneous monitoring of the SMR by the tracker as well as reference laser as the carriage was moved. Before carriage motion, the reference laser was reset at the desired initial position of the carriage along the rail. The IFM of the tracker was also set to zero at the same point using ADM by momentarily breaking the beam. The carriage was then moved and its final position recorded by both instruments. This measurement was repeated at increasing distances from the beam splitter.

7.5. MATHEMATICAL MODEL

The model described here involves environmental compensation for the reference laser using environmental data obtained from the tracker. Temperature probes on the bench

were not installed at the time of performing this experiment. As a result, only instrument self-compensation is used for the tracker. Table 7.1 shows the notations used in this model.

Table 7.1. Notations used in common path model

Notation	Description
d	Two point distance measured by tracker
$r_i, \theta_i, \emptyset_i$	Range, Azimuth and Zenith of point 'i' measured by tracker
$d\theta_i, d\emptyset_i$	Change in azimuth and zenith of point 'i' from point 1 measured by tracker
R	Displacement measured by reference interferometer
C	Atmospheric correction factor for reference interferometer
T, P, RH, Vp	Atmospheric conditions (Temperature, Pressure, Relative Humidity, Vapor pressure of water respectively)
K_t, K_p, K_h	Coefficient of refractive index change due to temperature, pressure and humidity respectively

$$d = \sqrt{r_1{}^2 + r_2{}^2 - 2r_1r_2\left(\sin\emptyset_1 \sin\emptyset_2 \cos(\theta_1 - \theta_2) + \cos\emptyset_1 \cos\emptyset_2\right)}$$

$$Measurand\ (Ranging\ error) = d - R.C$$

$$where\ C = 1 + K_t(T - 20) - K_p(P - 760) + K_h(V_p * RH - 10)$$

7.6. RESULTS AND DISCUSSION

Fig. 7.5 (a) shows the ranging errors estimated using the beam splitter method. Fig. 7.5 (b) shows the corresponding k=2 expanded uncertainties associated with these estimates.

The sources of uncertainty and their contributions for one of these measurements are shown in Table 7.2. Detailed uncertainty budgets for all measurements can be found in Appendix A.

(a)   (b)
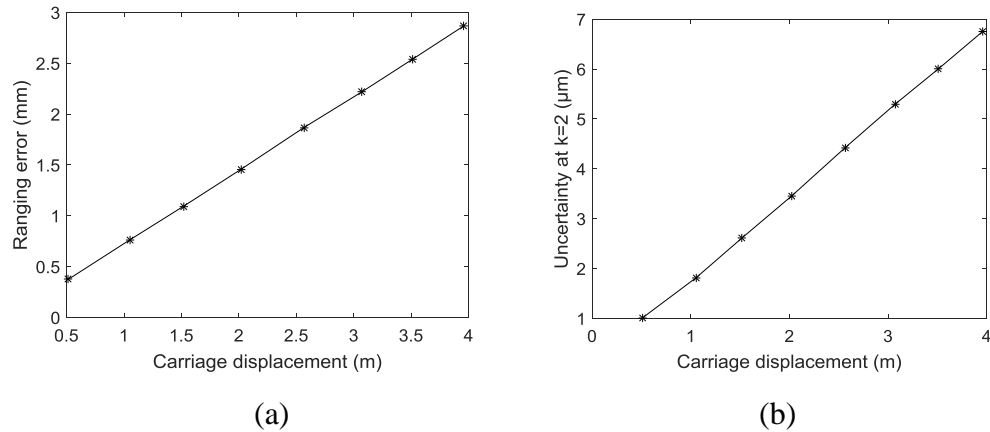
Fig. 7.5. Results of common path ranging test

.Table 7.2. Uncertainty contributors for common path ranging test

Contributor	Uncertainty contribution (µm)	Contributor		Uncertainty contribution (µm)
Range- point 1	0.92	Temperature		0.95
Range- point 2	1.02	Pressure		0.08
Azimuth- point 1	0.00	Relative humidity		0.10
Azimuth- point 2	0.00	Vapor pressure of water		0.01
Zenith- point 1	0.00	Coefficient of refractive index change due to	Temperature	0.00
Zenith- point 2	0.00		Pressure	0.00
Reference laser reading	1.01		Humidity	0.00

The ranging errors were observed to be of the order of millimeters. The source of these large errors is yet to be identified. For the case of the largest displacement of about 4 m, the difference between the carriage displacement reported by the self-compensated tracker and the uncompensated reference laser, was of the order of 2.8 mm. The process of compensation described by the correction factor shown in the model only resulted in a change of about 24 µm from the uncompensated value. Further, it was verified multiple times that the errors were not due to a manual error. It was interesting to note that such large errors did not show up in the back-to-back tests, where ranging errors are generally expected to be larger due to large dead paths.

Several attempts were therefore made to re-establish the setup for repeating the measurement to observe if these errors persisted. However, when attempting to track an SMR through the beam splitter, the tracker was unable to set the IFM zero via ADM though it was able to track it. As a result, range values continued to be reported to be zero, while variation of angular encoders with SMR motion verified that the tracker was able to track the target SMR. It was suspected that the tracker was being confused either be a return beam from the reference retroreflector or by a beam from the reference laser. However, no change was observed even when the reference retroreflector was removed and the reference laser was blocked from entering the beam splitter.

CHAPTER 8: FUTURE WORK

Work for the immediate future will include further attempts to investigate the source of the large errors observed with the common path method, and subsequent application of environmental compensation.

Additional future work in this area may include calibration of tapes and other artifacts, and possible development of a calibrated linear array of nests mounted on another rail capable of being attached to the guide rail of the bench. Such an apparatus could be used to evaluate the performance of instruments such as time-of-flight 3D scanners.

REFERENCES

[1] Sawyer, D., Borchardt, B., Phillips, S., Fronczek, C., Estler, T., Woo, W., et. al., 2002, A laser tracker calibration system, Proceedings of Measurement Science Conference, Anaheim, CA.

[2] ASME B89.4.19-2006 standard, Performance Evaluation of Laser-Based Spherical Coordinate Measurement Systems.

[3] Estler, W.T., Sawyer, D.S., Borchardt, B., and Phillips, S.D., 2006, Large-Scale Metrology Instrument Performance Evaluations at NIST, The Journal of the CMSC, 1/2:27–32.

[4] Blackburn, C., Sawyer, D., and Shakarji, C., 2014, Common-Path Method for Laser Tracker Ranging Calibration, The Journal of the CMSC, 9/1:4–7.

[5] Turolski, M., et. al., Linear Laser Performance: How distance, environment, and setup affect a laser tracker's Linear accuracy, The Journal of the CMSC, Autumn 2014, 30-33.

[6] Preston Thomas, H., The International Temperature Scale of 1990 (ITS-90), 1990, Metrologia 27, 3-10.

APPENDIX A: UNCERTAINTY BUDGETS

Table 1 shows the descriptions of symbols used in all uncertainty budgets listed in this appendix. Each table that follows represent the uncertainty budget corresponding to a particular measurement.

Table 1. Symbols used (common to all uncertainty budgets)

Symbol	Description
$r_i, \theta_i, \emptyset_i$	Range, azimuth and zenith of point 'i' measured by tracker
$d\theta_i, d\emptyset_i$	Change in azimuth and zenith of point i from point 1 measured by tracker
R	Carriage displacement measured by reference laser
T, P, RH	Temperature, pressure and relative humidity measured by tracker
T_r, P_r	Temperature, pressure measured by reference laser
T_p	Temperature measured by probes
V_p, V_{pr}, V_{pn}	Vapor pressure of water corresponding to temperatures T, T_r, and T_p
ΔT	Change in temperature measured by probes
K_t, K_p, K_h	Coefficient of refractive index change due to temperature, pressure and humidity

BALL BAR CALIBRATION

Tables 2-4 correspond to sets 1-3 described in Fig. 5.6. These show the uncertainty budgets for ball bar calibration when only instrument self-compensation was used.

Table 2. Budget for set 1- ball bar calibration

Component x_i	Mean $(\bar{x}_1)$	Standard uncertainty $u(x_i)$	Sensitivity coefficient $c_i = \partial f / \partial x_i$	Uncertainty contribution $u_i(f) = |c_i|u(x_i)$ μm
r_1	3.02 m	0.23 μm	-1.00	0.23
r_2	3.62 m	0.34 μm	1.00	0.34
θ_1	-0.28 rad	8.73 μrad	0.008	0.08
θ_2	-0.23 rad	8.73 μrad	-0.008	0.08
$\emptyset_1$	1.70 rad	8.73 μrad	-0.002	0.02
$\emptyset_2$	1.70 rad	8.73 μrad	0.002	0.02
$u_c(f) = \sqrt{\Sigma\, u_i^{\,2}(f)}$				0.43 μm
k=2 expanded uncertainty $U(f)$				0.86 μm

Table 3. Budget for set 2- ball bar calibration

Component x_i	Mean $(\bar{x}_1)$	Standard uncertainty $u(x_i)$	Sensitivity coefficient $c_i = \partial f / \partial x_i$	Uncertainty contribution $u_i(f) = |c_i|u(x_i)$ μm
r_1	7.27 m	0.48 μm	-1.00	0.48
r_2	7.87 m	0.49 μm	1.00	0.49
$\theta 1$	-0.23 rad	8.73 μrad	0.01	0.08
$\theta 2$	-0.23 rad	8.73 μrad	-0.01	0.08

Table 3 (continued)

Ø1	1.70 rad	8.73 μrad	-0.00	0.00
Ø2	1.70 rad	8.73 μrad	0.00	0.00
$u_c(f) = \sqrt{\Sigma\, u_i^{\,2}(f)}$				0.69 μm
k=2 expanded uncertainty $U(f)$				1.38 μm

Table 4. Budget for set 3- ball bar calibration

Component x_i	Mean $(\bar{x}_1)$	Standard uncertainty $u(x_i)$	Sensitivity coefficient $c_i = \partial f/\partial x_i$	Uncertainty contribution $u_i(f) = |c_i| u(x_i)$ μm
r_1	1.87 m	0.11 μm	0.65	0.07
r_2	1.56 m	0.17 μm	-0.40	0.07
θ_1	-0.95 rad	8.73 μrad	1.04	9.12
θ_2	-1.18 rad	8.73 μrad	-1.04	9.12
$\emptyset_1$	1.63 rad	8.73 μrad	-0.97	8.50
$\emptyset_2$	1.83 rad	8.73 μrad	0.94	8.16
$u_c(f) = \sqrt{\Sigma\, u_i^{\,2}(f)}$				17.47 μm
k=2 expanded uncertainty $U(f)$				35.94 μm

Tables 5-9 show the budgets for each measurement shown in Fig. 5.8.

Table 5. Budget for measurement 1 (1m from mirror)

Component x_i	Mean $(\bar{x}_1)$	Standard uncertainty $u(x_i)$	Sensitivity coefficient $c_i = \partial f / \partial x_i$	Uncertainty contribution $u_i(f) = |c_i|u(x_i)$ µm
r_1	5.16 m	0.05 µm	1.00	0.05
r_2	4.56 m	0.06 µm	-1.00	0.06
θ_1	0.02 rad	8.73 µrad	0.00	0.00
$d\theta_2$	-0.00 rad	0.35 µrad	-0.02	0.01
$\emptyset_1$	1.69 rad	8.73 µrad	-0.00	0.00
$d\emptyset_2$	-0.00 rad	0.29 µrad	-0.15	0.04
T	21.95 $^\circ$C	0.01 $^\circ$C	-0.00	0.00
P	750.94 mm Hg	0.11 mm Hg	-0.00	0.00
RH	0.45	0.05	-0.00	0.00
V_p	19.77 mm Hg	0.01 mm Hg	-0.00	0.00
T_p	21.68 $^\circ$C	0.50 $^\circ$C	-0.00	0.28
V_{pn}	19.45 mm Hg	0.50 mm Hg	0.00	0.01
ΔT	-0.02 $^\circ$C	0.30 $^\circ$C	-0.00	1.49
K_t	0.93 x 10^{-6}	10^{-10}	-0.16	0.00
K_p	0.36 x 10^{-6}	10^{-10}	0.00	0.00
K_h	0.05 x 10^{-6}	10^{-10}	-0.09	0.00
			$u_c(f) = \sqrt{\Sigma u_i^2(f)}$	1.52 µm
			k=2 expanded uncertainty $U(f)$	3.04 µm

Table 6. Budget for measurement 2 (2m from mirror)

Component x_i	Mean $(\bar{x}_i)$	Standard uncertainty $u(x_i)$	Sensitivity coefficient $c_i = \partial f/\partial x_i$	Uncertainty contribution $u_i(f) = |c_i|u(x_i)$ μm
r_1	6.14 m	0.07 μm	1.00	0.07
r_2	5.54 m	0.08 μm	-1.00	0.08
θ_1	0.02 rad	8.73 μrad	0.00	0.00
$d\theta_2$	-0.00 rad	0.41 μrad	-0.04	0.02
$\emptyset_1$	1.70 rad	8.73 μrad	-0.00	0.00
$d\emptyset_2$	-0.00 rad	0.38 μrad	-0.14	0.05
T	22.10 $^{\circ}$C	0.00 $^{\circ}$C	-0.00	0.00
P	749.37 mm Hg	0.10 mm Hg	-0.00	0.00
RH	0.43	0.05	-0.00	0.00
V_p	19.95 mm Hg	0.00 mm Hg	-0.00	0.00
T_p	21.14 $^{\circ}$C	0.51 $^{\circ}$C	-0.00	0.28
V_{pn}	20.00 mm Hg	0.50 mm Hg	0.00	0.01
ΔT	-0.09 $^{\circ}$C	0.30 $^{\circ}$C	-0.00	1.77
K_t	0.93 x 10^{-6}	10^{-10}	0.02	0.00
K_p	0.36 x 10^{-6}	10^{-10}	0.00	0.00
K_h	0.05 x 10^{-6}	10^{-10}	0.01	0.00
			$u_c(f) = \sqrt{\Sigma u_i^{\,2}(f)}$	1.80 μm
		k=2 expanded uncertainty $U(f)$		3.60μm

Table 7. Budget for measurement 3 (3m from mirror)

Component x_i	Mean $(\bar{x}_1)$	Standard uncertainty $u(x_i)$	Sensitivity coefficient $c_i = \partial f / \partial x_i$	Uncertainty contribution $u_i(f) = |c_i| u(x_i)$ μm
r_1	7.11 m	0.06 μm	1.00	0.06
r_2	6.51 m	0.16 μm	-1.00	0.16
θ_1	0.02 rad	8.73 μrad	0.00	0.00
$d\theta_2$	-0.00 rad	0.07 μrad	-0.02	0.01
$\emptyset_1$	1.70 rad	8.73 μrad	-0.00	0.00
$d\emptyset_2$	-0.00 rad	-0.47 μrad	-0.13	0.06
T	22.00 $^{\circ}$C	0.00 $^{\circ}$C	-0.00	0.00
P	749.34 mm Hg	0.11 mm Hg	-0.00	0.00
RH	0.43	0.05	-0.00	0.00
V_p	19.83 mm Hg	0.00 mm Hg	-0.00	0.00
T_p	21.09 $^{\circ}$C	0.52 $^{\circ}$C	0.00	0.29
V_{pn}	18.75 mm Hg	0.50 mm Hg	0.00	0.01
ΔT	-0.18 $^{\circ}$C	0.30 $^{\circ}$C	-0.00	2.06
K_t	0.93 x 10^{-6}	10^{-10}	-0.55	0.00
K_p	0.36 x 10^{-6}	10^{-10}	0.00	0.00
K_h	0.05 x 10^{-6}	10^{-10}	-0.28	0.00
			$u_c(f) = \sqrt{\Sigma u_i^2 (f)}$	2.09 μm
			k=2 expanded uncertainty $U(f)$	4.18 μm

Table 8. Budget for measurement 4 (4m from mirror)

Component x_i	Mean $(\bar{x}_i)$	Standard uncertainty $u(x_i)$	Sensitivity coefficient $c_i = \partial f/\partial x_i$	Uncertainty contribution $u_i(f) = |c_i|u(x_i)$ µm
r_1	8.11 m	0.05 µm	1.00	0.05
r_2	7.51 m	0.17 µm	-1.00	0.17
θ_1	0.02 rad	8.73 µrad	0.00	0.00
$d\theta_2$	-0.00 rad	0.40 µrad	-0.06	0.02
$\emptyset_1$	1.71 rad	8.73 µrad	-0.00	0.00
$d\emptyset_2$	-0.00 rad	0.25 µrad	-0.13	0.03
T	21.85 $^{\circ}$C	0.01 $^{\circ}$C	-0.00	0.00
P	749.35 mm Hg	0.11 mm Hg	-0.00	0.00
RH	0.43	0.05	-0.00	0.00
V_p	19.65 mm Hg	0.01 mm Hg	-0.00	0.00
T_p	21.70 $^{\circ}$C	0.53 $^{\circ}$C	-0.00	0.30
V_{pn}	19.47 mm Hg	0.51 mm Hg	0.00	0.01
ΔT	0.27 $^{\circ}$C	0.31 $^{\circ}$C	-0.00	2.41
K_t	0.93 x 10^{-6}	10^{-10}	-0.09	0.00
K_p	0.36 x 10^{-6}	10^{-10}	0.00	0.00
K_h	0.05 x 10^{-6}	10^{-10}	-0.05	0.00
			$u_c(f) = \sqrt{\Sigma u_i^2(f)}$	2.43 µm
			k=2 expanded uncertainty $U(f)$	4.86 µm

Table 9. Budget for measurement 5 (5m from mirror)

Component x_i	Mean $(\bar{x}_1)$	Standard uncertainty $u(x_i)$	Sensitivity coefficient $c_i = \partial f / \partial x_i$	Uncertainty contribution $u_i(f) = |c_i|u(x_i)$ μm
r_1	9.11 m	0.18 μm	1.00	0.18
r_2	8.51 m	0.38 μm	-1.00	0.38
θ_1	0.02 rad	8.74 μrad	0.00	0.00
$d\theta_2$	-0.00 rad	0.50 μrad	-0.02	0.01
$\emptyset_1$	1.71 rad	8.74 μrad	-0.00	0.00
$d\emptyset_2$	-0.00 rad	0.28 μrad	-0.11	0.03
T	22.18 $^{\circ}$C	0.02 $^{\circ}$C	-0.00	0.01
P	749.35 mm Hg	0.11 mm Hg	-0.00	0.00
RH	0.42	0.05	0.00	0.00
V_p	20.05 mm Hg	0.02 mm Hg	-0.00	0.00
T_p	22.93 $^{\circ}$C	0.51 $^{\circ}$C	-0.00	0.29
V_{pn}	20.99 mm Hg	0.52 mm Hg	0.00	0.01
ΔT	0.07 $^{\circ}$C	0.31 $^{\circ}$C	-0.00	2.69
K_t	0.93 x 10^{-6}	10^{-10}	0.45	0.00
K_p	0.36 x 10^{-6}	10^{-10}	-0.00	0.00
K_h	0.05 x 10^{-6}	10^{-10}	0.24	0.00
			$u_c(f) = \sqrt{\Sigma u_i^2(f)}$	2.74 μm
			k=2 expanded uncertainty $U(f)$	5.48 μm

BACK-TO-BACK TEST- FOUR POINT METHOD

Tables 10-13 show the uncertainty budgets for measurements 1-4 of Fig. 6.6.

Table 10. Budget for measurement 1

Component x_i	Mean $(\bar{x}_1)$	Standard uncertainty $u(x_i)$	Sensitivity coefficient $c_i = \partial f / \partial x_i$	Uncertainty contribution $u_i(f) = |c_i|u(x_i)$ μm
r_1	6.72 m	0.00 μm	0.00	0.00
r_2	6.67 m	0.15 μm	-1.00	0.15
r_3	7.11 m	0.29 μm	1.00	0.29
r_4	7.16 m	0.27 μm	0.00	0.00
θ_1	-2.55 rad	8.74 μrad	0.00	0.00
$d\theta_2$	0.00 rad	0.65 μrad	-0.04	0.03
$d\theta_3$	0.00 rad	0.77 μrad	0.04	0.04
$d\theta_4$	0.00 rad	0.58 μrad	-0.04	0.03
$\emptyset_1$	1.68 rad	8.74 μrad	-0.00	0.00
$d\emptyset_2$	0.00 rad	0.53 μrad	-0.42	0.22
$d\emptyset_3$	0.00 rad	0.62 μrad	0.45	0.28
$d\emptyset_4$	0.00 rad	0.71 μrad	-0.45	0.32
R	0.44 m	0.22 μm	-1.00	0.22
T	21.84 $^\circ$ C	1.01 $^\circ$ C	-0.00	0.41
P	744.63 mm Hg	0.11 mm Hg	-0.00	0.02
RH	0.37	0.05	-0.00	0.02
V_p	19.64 mm Hg	1.01 mm Hg	-0.00	0.01
K_t	0.93 x 10^{-6}	10^{-10}	-0.81	0.00
K_p	0.36 x 10^{-6}	10^{-10}	-6.79	0.00
K_h	0.05 x 10^{-6}	10^{-10}	1.25	0.00
$u_c(f) = \sqrt{\Sigma u_i^2(f)}$				0.75 μm
k=2 expanded uncertainty $U(f)$				1.50 μm

Table 11. Budget for measurement 2

Component x_i	Mean $(\bar{x}_i)$	Standard uncertainty $u(x_i)$	Sensitivity coefficient $c_i = \partial f / \partial x_i$	Uncertainty contribution $u_i(f) = |c_i| u(x_i)$ μm
r_1	6.71 m	0.27 μm	0.00	0.00
r_2	6.66 m	0.11 μm	-1.00	0.11
r_3	7.07 m	0.22 μm	1.00	0.22
r_4	7.12 m	0.25 μm	-0.00	0.00
θ_1	-2.55 rad	8.73 μrad	0.00	0.00
$d\theta_2$	0.00 rad	0.40 μrad	-0.04	0.02
$d\theta_3$	0.00 rad	0.62 μrad	0.05	0.03
$d\theta_4$	0.00 rad	0.37 μrad	-0.04	0.02
$\emptyset_1$	1.68 rad	8.73 μrad	-0.00	0.00
$d\emptyset_2$	0.00 rad	0.44 μrad	-0.42	0.19
$d\emptyset_3$	0.00 rad	0.37 μrad	0.45	0.16
$d\emptyset_4$	0.00 rad	0.47 μrad	-0.45	0.22
R	0.41 m	0.21 μm	-1.00	0.21
T	22.01 $^\circ$ C	1.01 $^\circ$ C	-0.00	0.38
P	744.86 mm Hg	0.10 mm Hg	-0.00	0.02
RH	0.35	0.05	-0.00	0.02
V_p	19.85 mm Hg	1.01 mm Hg	-0.00	0.01
K_t	0.93 x 10^{-6}	10^{-10}	-0.82	0.00
K_p	0.36 x 10^{-6}	10^{-10}	-6.14	0.00
K_h	0.05 x 10^{-6}	10^{-10}	1.20	0.00
			$u_c(f) = \sqrt{\Sigma\, u_i^{\,2}(f)}$	0.60 μm
			k=2 expanded uncertainty $U(f)$	1.20 μm

Table 12. Budget for measurement 3

Component x_i	Mean $(\bar{x}_i)$	Standard uncertainty $u(x_i)$	Sensitivity coefficient $c_i = \partial f / \partial x_i$	Uncertainty contribution $u_i(f) = \lvert c_i \rvert u(x_i)$ μm
r_1	6.72 m	0.32 μm	0.00	0.00
r_2	6.67 m	0.15 μm	-1.00	0.15
r_3	6.95 m	0.19 μm	1.00	0.29
r_4	7.00 m	0.43 μm	-0.00	0.00
θ_1	-2.55 rad	8.73 μrad	0.00	0.00
$d\theta_2$	0.00 rad	0.45 μrad	-0.04	0.03
$d\theta_3$	0.00 rad	0.45 μrad	0.05	0.04
$d\theta_4$	0.00 rad	0.52 μrad	-0.04	0.03
$\emptyset_1$	1.68 rad	8.73 μrad	-0.00	0.00
$d\emptyset_2$	0.00 rad	0.40 μrad	-0.42	0.22
$d\emptyset_3$	0.00 rad	0.33 μrad	0.44	0.28
$d\emptyset_4$	0.00 rad	0.61 μrad	-0.45	0.32
R	0.28 m	0.16 μm	-1.00	0.22
T	21.76 ^{o} C	1.01 ^{o} C	-0.00	0.41
P	744.87 mm Hg	0.11 mm Hg	0.00	0.02
RH	0.36	0.05	-0.00	0.02
V_p	19.54 mm Hg	1.01 mm Hg	-0.00	0.01
K_t	0.93 x 10^{-6}	10^{-10}	-0.49	0.00
K_p	0.36 x 10^{-6}	10^{-10}	-4.20	0.00
K_h	0.05 x 10^{-6}	10^{-10}	0.83	0.00
			$u_c(f) = \sqrt{\Sigma\, u_i^{\,2}(f)}$	0.53 μm
			k=2 expanded uncertainty $U(f)$	1.06 μm

Table 13. Budget for measurement 4

Component x_i	Mean $(\bar{x}_i)$	Standard uncertainty $u(x_i)$	Sensitivity coefficient $c_i = \partial f / \partial x_i$	Uncertainty contribution $u_i(f) = |c_i| u(x_i)$ μm
r_1	6.72 m	0.50 μm	0.00	0.00
r_2	6.67 m	0.08 μm	-1.00	0.08
r_3	7.18 m	0.36 μm	1.00	0.37
r_4	7.23 m	0.31 μm	-0.00	0.00
θ_1	-2.55 rad	8.73 μrad	0.00	0.00
$d\theta_2$	0.00 rad	0.27 μrad	-0.04	0.01
$d\theta_3$	0.00 rad	0.39 μrad	0.05	0.02
$d\theta_4$	0.00 rad	0.40 μrad	-0.05	0.02
$\emptyset_1$	1.68 rad	8.73 μrad	-0.00	0.00
$d\emptyset_2$	0.00 rad	0.40 μrad	-0.42	0.17
$d\emptyset_3$	0.00 rad	0.33 μrad	0.45	0.15
$d\emptyset_4$	0.00 rad	0.36 μrad	-0.46	0.17
R	0.51 m	0.27 μm	-1.00	0.27
T	21.75 $^\circ$ C	1.01 $^\circ$ C	-0.00	0.47
P	744.57 mm Hg	0.10 mm Hg	0.00	0.02
RH	0.36	0.05	-0.00	0.02
V_p	19.53 mm Hg	1.01 mm Hg	-0.00	0.01
K_t	0.93 x 10^{-6}	10^{-10}	-0.88	0.00
K_p	0.36 x 10^{-6}	10^{-10}	-7.79	0.00
K_h	0.05 x 10^{-6}	10^{-10}	1.45	0.00
			$u_c(f) = \sqrt{\Sigma u_i^2(f)}$	0.72 μm
			k=2 expanded uncertainty $U(f)$	1.44 μm

APPENDIX H

BACK-TO-BACK TEST- TWO POINT METHOD

Tables 14-22 show the uncertainty budgets for measurements 1-9 of Fig. 6.7.

Table 14. Budget for measurement 1

Component x_i	Mean $(\bar{x}_1)$	Standard uncertainty $u(x_i)$	Sensitivity coefficient $c_i = \partial f / \partial x_i$	Uncertainty contribution $u_i(f) = |c_i|u(x_i)$ μm
r_1	8.48 m	0.88 μm	0.99	0.88
r_2	7.99 m	1.02 μm	-0.99	1.01
θ_1	-1.96 rad	8.76 μrad	0.00	0.00
$d\theta_2$	0.01 rad	1.39 μrad	1.09	1.52
$\emptyset_1$	1.69 rad	8.75 μrad	-0.00	0.01
$d\emptyset_2$	0.00 rad	0.84 μrad	0.05	0.04
R	0.50 m	0.09 μm	-1.00	0.09
T	21.86 $^{\circ}$C	0.01 $^{\circ}$C	-0.00	0.01
P	751.00 mm Hg	0.11 mm Hg	0.00	0.02
RH	0.45	0.05	-0.00	0.02
V_p	19.66 mm Hg	0.01 mm Hg	-0.00	0.00
T_p	21.59 $^{\circ}$C	1.00 $^{\circ}$C	-0.00	0.01
V_{pn}	19.34 mm Hg	1.01 mm Hg	-0.00	0.00
T_r	22.00 $^{\circ}$C	0.01 $^{\circ}$C	0.00	0.01
P_r	736.00 mm Hg	0.11 mm Hg	-0.00	0.02
V_{pr}	19.83 mm Hg	0.01 mm Hg	0.00	0.00
ΔT	-0.12 $^{\circ}$C	0.30 $^{\circ}$C	-0.00	2.42
K_t	0.93 x 10^{-6}	10^{-10}	0.08	0.00
K_p	0.36 x 10^{-6}	10^{-10}	7.50	0.00
K_h	0.05 x 10^{-6}	10^{-10}	0.53	0.00
$u_c(f) = \sqrt{\Sigma u_i^{~2}(f)}$				3.16 μm
k=2 expanded uncertainty $U(f)$				6.32 μm

Table 15. Budget for measurement 2

Component x_i	Mean $(\bar{x}_i)$	Standard uncertainty $u(x_i)$	Sensitivity coefficient $c_i = \partial f/\partial x_i$	Uncertainty contribution $u_i(f) = |c_i|u(x_i)$ μm
r_1	8.50 m	0.92 μm	0.99	0.92
r_2	7.49 m	0.96 μm	-0.99	0.95
θ_1	-1.96 rad	8.77 μrad	0.00	0.00
$d\theta_2$	0.02 rad	0.92 μrad	1.09	1.01
$\emptyset_1$	1.69 rad	8.77 μrad	-0.00	0.02
$d\emptyset_2$	0.00 rad	0.87 μrad	0.05	0.04
R	1.02 m	0.05 μm	-1.00	0.05
T	21.75 $^\circ$C	0.01 $^\circ$C	-0.00	0.01
P	750.96 mm Hg	0.10 mm Hg	0.00	0.04
RH	0.46	0.05	-0.00	0.05
V_p	19.53 mm Hg	0.01 mm Hg	-0.00	0.00
T_p	21.45 $^\circ$C	1.00 $^\circ$C	-0.00	0.02
V_{pn}	19.18 mm Hg	1.01 mm Hg	-0.00	0.00
T_r	21.94 $^\circ$C	0.01 $^\circ$C	0.00	0.01
P_r	735.80 mm Hg	0.10 mm Hg	-0.00	0.04
V_{pr}	19.76 mm Hg	0.01 mm Hg	0.00	0.00
ΔT	0.04 $^\circ$C	0.30 $^\circ$C	-0.00	2.43
K_t	0.93 x 10^{-6}	10^{-10}	0.20	0.00
K_p	0.36 x 10^{-6}	10^{-10}	15.49	0.00
K_h	0.05 x 10^{-6}	10^{-10}	1.01	0.00
$u_c(f) = \sqrt{\Sigma u_i^2(f)}$				2.95 μm
k=2 expanded uncertainty $U(f)$				5.90 μm

Table 16. Budget for measurement 3

Component x_i	Mean $(\bar{x}_1)$	Standard uncertainty $u(x_i)$	Sensitivity coefficient $c_i = \partial f / \partial x_i$	Uncertainty contribution $u_i(f) = |c_i| u(x_i)$ μm
r_1	8.50 m	0.82 μm	0.99	0.88
r_2	7.00 m	1.00 μm	-0.99	1.00
θ_1	-1.96 rad	8.76 μrad	0.00	0.00
$d\theta_2$	0.03 rad	1.26 μrad	1.09	1.37
$\emptyset_1$	1.69 rad	8.74 μrad	-0.00	0.03
$d\emptyset_2$	0.00 rad	0.41 μrad	0.05	0.02
R	1.52 m	0.18 μm	-1.00	0.18
T	21.70 $^\circ$ C	0.00 $^\circ$ C	-0.00	0.00
P	750.99 mm Hg	0.11 mm Hg	0.00	0.06
RH	0.46	0.05	-0.00	0.07
V_p	19.47 mm Hg	0.00 mm Hg	-0.00	0.00
T_p	21.37 $^\circ$ C	1.01 $^\circ$ C	-0.00	0.03
V_{pn}	19.08 mm Hg	1.00 mm Hg	-0.00	0.00
T_r	21.89 $^\circ$ C	0.00 $^\circ$ C	0.00	0.00
P_r	735.80 mm Hg	0.11 mm Hg	-0.00	0.06
V_{pr}	19.70 mm Hg	0.00 mm Hg	0.00	0.00
ΔT	-0.09 $^\circ$ C	0.36 $^\circ$ C	-0.00	2.87
K_t	0.93 x 10^{-6}	10^{-10}	0.30	0.00
K_p	0.36 x 10^{-6}	10^{-10}	23.02	0.00
K_h	0.05 x 10^{-6}	10^{-10}	1.42	0.00
$u_c(f) = \sqrt{\Sigma u_i^2(f)}$				3.44 μm
k=2 expanded uncertainty $U(f)$				6.88 μm

Table 17. Budget for measurement 4

Component x_i	Mean $(\bar{x}_1)$	Standard uncertainty $u(x_i)$	Sensitivity coefficient $c_i = \partial f / \partial x_i$	Uncertainty contribution $u_i(f) = |c_i| u(x_i)$ μm
r_1	8.50 m	0.96 μm	0.99	0.95
r_2	6.51 m	0.76 μm	-0.99	0.75
θ_1	-1.96 rad	8.77 μrad	0.00	0.00
$d\theta_2$	0.04 rad	1.08 μrad	1.09	1.18
$\emptyset_1$	1.69 rad	8.80 μrad	-0.01	0.04
$d\emptyset_2$	0.00 rad	1.31 μrad	0.05	0.06
R	2.00 m	0.14 μm	-1.00	0.14
T	21.61 $^\circ$C	0.01 $^\circ$C	-0.00	0.01
P	70.92 mm Hg	0.11 mm Hg	0.00	0.08
RH	0.46	0.05	-0.00	0.10
V_p	19.36 mm Hg	0.01 mm Hg	-0.00	0.00
T_p	21.27 $^\circ$C	1.04 $^\circ$C	-0.00	0.05
V_{pn}	18.97 mm Hg	1.01 mm Hg	-0.00	0.00
T_r	21.82 $^\circ$C	0.01 $^\circ$C	0.00	0.01
P_r	735.90 mm Hg	0.11 mm Hg	-0.00	0.08
V_{pr}	19.62 mm Hg	0.01 mm Hg	0.00	0.00
ΔT	-0.06 $^\circ$C	0.30 $^\circ$C	-0.00	2.42
K_t	0.93 x 10^{-6}	10^{-10}	0.45	0.00
K_p	0.36 x 10^{-6}	10^{-10}	30.13	0.00
K_h	0.05 x 10^{-6}	10^{-10}	1.75	0.00
$u_c(f) = \sqrt{\Sigma\, u_i^{\,2}(f)}$				2.95 μm
k=2 expanded uncertainty $U(f)$				5.90 μm

Table 18. Budget for measurement 5

Component x_i	Mean $(\bar{x}_i)$	Standard uncertainty $u(x_i)$	Sensitivity coefficient $c_i = \partial f/\partial x_i$	Uncertainty contribution $u_i(f) = |c_i|u(x_i)$ μm
r_1	8.50 m	0.51 μm	0.99	0.51
r_2	6.01 m	1.14 μm	-0.98	1.12
θ_1	-1.96 rad	8.74 μrad	0.00	0.00
$d\theta_2$	0.05 rad	1.23 μrad	1.10	1.35
$\emptyset_1$	1.69 rad	8.73 μrad	-0.01	0.06
$d\emptyset_2$	0.00 rad	1.36 μrad	0.04	0.06
R	2.51 m	0.02 μm	-1.00	0.02
T	21.55 °C	0.01 °C	-0.00	0.03
P	750.96 mm Hg	0.10 mm Hg	0.00	0.09
RH	0.46	0.05	-0.00	0.12
V_p	19.30 mm Hg	0.01 mm Hg	-0.00	0.00
T_p	21.11 °C	1.19 °C	-0.00	0.08
V_{pn}	18.78 mm Hg	1.01 mm Hg	-0.00	0.00
T_r	21.76 °C	0.01 °C	0.00	0.03
P_r	735.80 mm Hg	0.11 mm Hg	-0.00	0.09
V_{pr}	19.55 mm Hg	0.01 mm Hg	0.00	0.00
ΔT	0.00 °C	0.30 °C	-0.00	2.41
K_t	0.93 x 10^{-6}	10^{-10}	0.56	0.00
K_p	0.36 x 10^{-6}	10^{-10}	38.08	0.00
K_h	0.05 x 10^{-6}	10^{-10}	2.21	0.00
$u_c(f) = \sqrt{\Sigma u_i^2(f)}$				3.03 μm
k=2 expanded uncertainty $U(f)$				6.06 μm

Table 19. Budget for measurement 6

Component x_i	Mean $(\bar{x}_i)$	Standard uncertainty $u(x_i)$	Sensitivity coefficient $c_i = \partial f/\partial x_i$	Uncertainty contribution $u_i(f) = |c_i|u(x_i)$ μm
r_1	8.50 m	0.47 μm	0.99	0.46
r_2	5.54 m	0.79 μm	-0.98	0.77
θ_1	-1.96 rad	8.74 μrad	0.00	0.00
$d\theta_2$	0.07 rad	0.69 μrad	1.10	0.76
$\emptyset_1$	1.69 rad	8.73 μrad	-0.01	0.08
$d\emptyset_2$	0.00 rad	0.59 μrad	0.04	0.03
R	2.99 m	0.38 μm	-1.00	0.38
T	21.79 $^\circ$C	0.02 $^\circ$C	-0.00	0.06
P	752.80 mm Hg	0.11 mm Hg	0.00	0.12
RH	0.47	0.05	-0.00	0.15
V_p	19.58 mm Hg	0.03 mm Hg	-0.00	0.00
T_p	22.31 $^\circ$C	1.08 $^\circ$C	-0.00	0.10
V_{pn}	20.21 mm Hg	1.03 mm Hg	-0.00	0.00
T_r	21.83 $^\circ$C	1.02 $^\circ$C	0.00	0.07
P_r	737.60 mm Hg	0.11 mm Hg	-0.00	0.12
V_{pr}	19.63 mm Hg	0.03 mm Hg	0.00	0.00
ΔT	0.12 $^\circ$C	0.40 $^\circ$C	-0.00	3.22
K_t	0.93 x 10^{-6}	10^{-10}	0.07	0.00
K_p	0.36 x 10^{-6}	10^{-10}	45.50	0.00
K_h	0.05 x 10^{-6}	10^{-10}	1.51	0.00
$u_c(f) = \sqrt{\Sigma u_i^2(f)}$				3.46 μm
k=2 expanded uncertainty $U(f)$				6.92 μm

Table 20. Budget for measurement 7

Component x_i	Mean $(\bar{x}_i)$	Standard uncertainty $u(x_i)$	Sensitivity coefficient $c_i = \partial f/\partial x_i$	Uncertainty contribution $u_i(f) = |c_i|u(x_i)$ μm
r_1	8.48 m	0.41 μm	0.99	0.88
r_2	5.03 m	1.34 μm	-0.98	1.01
θ_1	-1.96 rad	8.74 μrad	0.00	0.00
$d\theta_2$	0.09 rad	0.95 μrad	1.10	1.52
$\emptyset_1$	1.69 rad	8.73 μrad	-0.01	0.01
$d\emptyset_2$	0.00 rad	0.46 μrad	0.04	0.04
R	3.50 m	1.17 μm	-1.00	0.09
T	22.06 $^{\circ}$C	0.01 $^{\circ}$C	-0.00	0.01
P	752.87 mm Hg	0.11 mm Hg	0.00	0.02
RH	0.47	0.05	-0.00	0.02
V_p	19.91 mm Hg	0.01 mm Hg	-0.00	0.00
T_p	22.06 $^{\circ}$C	1.16 $^{\circ}$C	-0.00	0.01
V_{pn}	19.91 mm Hg	1.01 mm Hg	-0.00	0.00
T_r	21.95 $^{\circ}$C	0.01 $^{\circ}$C	0.00	0.01
P_r	737.70 mm Hg	0.11 mm Hg	-0.00	0.02
V_{pr}	19.77 mm Hg	0.01 mm Hg	0.00	0.00
ΔT	-0.33 $^{\circ}$C	0.35 $^{\circ}$C	-0.00	2.42
K_t	0.93 x 10^{-6}	10^{-10}	-0.39	0.00
K_p	0.36 x 10^{-6}	10^{-10}	53.091	0.01
K_h	0.05 x 10^{-6}	10^{-10}	1.97	0.00
$u_c(f) = \sqrt{\Sigma\, u_i^{\,2}(f)}$				3.52 μm
k=2 expanded uncertainty $U(f)$				7.04 μm

Table 21. Budget for measurement 8

Component x_i	Mean $(\bar{x}_i)$	Standard uncertainty $u(x_i)$	Sensitivity coefficient $c_i = \partial f / \partial x_i$	Uncertainty contribution $u_i(f) = |c_i|u(x_i)$ μm
r_1	8.50 m	0.78 μm	0.99	0.77
r_2	4.60 m	0.87 μm	-0.97	0.85
θ_1	-1.96 rad	8.75 μrad	0.00	0.00
$d\theta_2$	0.11 rad	0.68 μrad	1.10	0.74
$\emptyset_1$	1.69 rad	0.09 μrad	-0.01	0.13
$d\emptyset_2$	0.00 rad	0.64 μrad	0.04	0.02
R	3.96 m	0.69 μm	-1.00	0.69
T	22.05 $^\circ$ C	0.01 $^\circ$ C	-0.00	0.04
P	752.84 mm Hg	0.12 mm Hg	0.00	0.17
RH	0.47	0.05	-0.00	0.20
V_p	19.89 mm Hg	0.01 mm Hg	-0.00	0.00
T_p	21.71 $^\circ$ C	1.23 $^\circ$ C	-0.00	0.20
V_{pn}	19.48 mm Hg	1.01 mm Hg	-0.00	0.00
T_r	21.98 $^\circ$ C	0.01 $^\circ$ C	0.00	0.04
P_r	737.60 mm Hg	0.11 mm Hg	-0.00	0.17
V_{pr}	19.81 mm Hg	0.01 mm Hg	0.00	0.00
ΔT	-0.15 $^\circ$ C	0.31 $^\circ$ C	-0.00	2.45
K_t	0.93 x 10^{-6}	10^{-10}	-0.20	0.00
K_p	0.36 x 10^{-6}	10^{-10}	60.38	0.01
K_h	0.05 x 10^{-6}	10^{-10}	2.03	0.00
$u_c(f) = \sqrt{\Sigma u_i^2(f)}$				2.91 μm
k=2 expanded uncertainty $U(f)$				5.82 μm

Table 22. Budget for measurement 9

Component x_i	Mean $(\bar{x}_i)$	Standard uncertainty $u(x_i)$	Sensitivity coefficient $c_i = \partial f/\partial x_i$	Uncertainty contribution $u_i(f) = |c_i|u(x_i)$ μm
r_1	8.50 m	0.75 μm	0.99	0.75
r_2	4.05 m	1.28 μm	-0.96	1.23
θ_1	-1.96 rad	8.75 μrad	0.00	0.00
$d\theta_2$	0.15 rad	1.13 μrad	1.10	1.24
$\emptyset_1$	1.69 rad	8.75 μrad	-0.02	0.17
$d\emptyset_2$	0.01 rad	0.61 μrad	0.03	0.02
R	4.53 m	0.80 μm	-1.00	0.80
T	21.93 °C	0.01 °C	-0.00	0.04
P	752.84 mm Hg	0.10 mm Hg	0.00	0.17
RH	0.48	0.05	-0.00	0.22
V_p	19.74 mm Hg	0.01 mm Hg	-0.00	0.00
T_p	21.48 °C	1.15 °C	-0.00	0.27
V_{pn}	19.21 mm Hg	1.01 mm Hg	-0.00	0.01
T_r	21.98 °C	0.01 °C	0.00	0.04
P_r	737.60 mm Hg	0.10 mm Hg	-0.00	0.17
V_{pr}	19.81 mm Hg	0.01 mm Hg	0.00	0.00
ΔT	-0.17 °C	0.31 °C	-0.00	2.46
K_t	0.93 x 10^{-6}	10^{-10}	0.36	0.00
K_p	0.36 x 10^{-6}	10^{-10}	69.09	0.01
K_h	0.05 x 10^{-6}	10^{-10}	2.33	0.00
$u_c(f) = \sqrt{\Sigma\, u_i^{\,2}(f)}$				3.24 μm
k=2 expanded uncertainty $U(f)$				6.48 μm

COMMON PATH TEST- BEAM SPLITTER METHOD

Tables 23-30 show the uncertainty budgets for measurements 1-8 of Fig. 7.5.

Table 23. Budget for measurement 1

Component x_i	Mean $(\bar{x}_1)$	Standard uncertainty $u(x_i)$	Sensitivity coefficient $c_i = \partial f / \partial x_i$	Uncertainty contribution $u_i(f) = |c_i|u(x_i)$ μm
r_1	2.76 m	0.12 μm	-1.00	0.12
r_2	3.27 m	0.33 μm	1.00	0.33
θ_1	-1.07 rad	8.73 μrad	0.00	0.00
$d\theta_2$	0.00 rad	0.28 μrad	0.00	0.00
$\emptyset_1$	1.71 rad	8.74 μrad	-0.00	0.00
$d\emptyset_2$	-0.00 rad	0.62 μrad	-0.00	0.00
R	0.51 m	0.26 μm	-1.00	0.26
T	22.01 ^{o} C	0.52 ^{o} C	-0.00	0.25
P	747.91 mm Hg	0.11 mm Hg	0.00	0.02
RH	0.19	0.05	-0.00	0.03
V_p	19.84 mm Hg	0.52 mm Hg	-0.00	0.00
K_t	0.93 x 10^{-6}	10^{-10}	-1.03	0.00
K_p	0.36 x 10^{-6}	10^{-10}	-6.21	0.00
K_h	0.05 x 10^{-6}	10^{-10}	3.19	0.00
			$u_c(f) = \sqrt{\Sigma u_i^2(f)}$	0.51 μm
			k=2 expanded uncertainty $U(f)$	1.02 μm

Table 24. Budget for measurement 2

Component x_i	Mean $(\bar{x}_1)$	Standard uncertainty $u(x_i)$	Sensitivity coefficient $c_i = \partial f/\partial x_i$	Uncertainty contribution $u_i(f) = |c_i|u(x_i)$ μm
r_1	2.75 m	0.14 μm	-1.00	0.14
r_2	3.81 m	0.53 μm	1.00	0.53
θ_1	-1.07 rad	8.73 μrad	0.00	0.00
$d\theta_2$	0.00 rad	0.44 μrad	0.00	0.00
$\emptyset_1$	1.71 rad	8.74 μrad	-0.00	0.00
$d\emptyset_2$	-0.00 rad	0.42 μrad	-0.00	0.00
R	1.05 m	0.53 μm	-1.00	0.53
T	22.48 $^\circ$C	0.51 $^\circ$C	-0.00	0.49
P	747.93 mm Hg	0.11 mm Hg	0.00	0.04
RH	0.18	0.05	-0.00	0.05
V_p	20.42 mm Hg	0.51 mm Hg	-0.00	0.00
K_t	0.93 x 10^{-6}	10^{-10}	-2.60	0.00
K_p	0.36 x 10^{-6}	10^{-10}	-12.70	0.00
K_h	0.05 x 10^{-6}	10^{-10}	6.59	0.00
			$u_c(f) = \sqrt{\Sigma u_i{}^2(f)}$	0.91 μm
			k=2 expanded uncertainty $U(f)$	1.82 μm

Table 25. Budget for measurement 3

Component x_i	Mean $(\bar{x}_1)$	Standard uncertainty $u(x_i)$	Sensitivity coefficient $c_i = \partial f / \partial x_i$	Uncertainty contribution $u_i(f) = |c_i|u(x_i)$ μm
r_1	2.60 m	0.09 μm	-1.00	0.09
r_2	4.12 m	0.77 μm	1.00	0.77
θ_1	-1.07 rad	8.73 μrad	0.00	0.00
$d\theta_2$	0.00 rad	0.42 μrad	0.00	0.00
$\emptyset_1$	1.71 rad	8.73 μrad	-0.00	0.00
$d\emptyset_2$	-0.00 rad	0.39 μrad	-0.00	0.00
R	1.52 m	0.76 μm	-1.00	0.76
T	22.17 $^\circ$ C	0.51 $^\circ$ C	-0.00	0.72
P	747.99 mm Hg	0.10 mm Hg	0.00	0.06
RH	0.19	0.05	-0.00	0.08
V_p	20.04 mm Hg	0.51 mm Hg	-0.00	0.01
K_t	0.93 x 10^{-6}	10^{-10}	-3.29	0.00
K_p	0.36 x 10^{-6}	10^{-10}	-18.20	0.00
K_h	0.05 x 10^{-6}	10^{-10}	9.52	0.00
			$u_c(f) = \sqrt{\Sigma u_i^2(f)}$	1.31 μm
			k=2 expanded uncertainty $U(f)$	2.62 μm

Table 26. Budget for measurement 4

Component x_i	Mean $(\bar{x}_1)$	Standard uncertainty $u(x_i)$	Sensitivity coefficient $c_i = \partial f / \partial x_i$	Uncertainty contribution $u_i(f) = |c_i| u(x_i)$ μm
r_1	2.60 m	0.09 μm	-1.00	0.09
r_2	4.62 m	1.02 μm	1.00	1.02
θ_1	-1.07 rad	8.73 μrad	0.00	0.00
$d\theta_2$	0.00 rad	0.41 μrad	0.00	0.00
$\emptyset_1$	1.71 rad	8.74 μrad	-0.00	0.00
$d\emptyset_2$	-0.00 rad	0.57 μrad	-0.00	0.00
R	2.02 m	1.01 μm	-1.00	1.01
T	21.95 $^\circ$C	0.51 $^\circ$C	-0.00	0.95
P	747.98 mm Hg	0.10 mm Hg	0.00	0.08
RH	0.19	0.05	-0.00	0.10
V_p	19.77 mm Hg	0.51 mm Hg	-0.00	0.01
K_t	0.93 x 10^{-6}	10^{-10}	-3.93	0.00
K_p	0.36 x 10^{-6}	10^{-10}	-24.25	0.00
K_h	0.05 x 10^{-6}	10^{-10}	12.68	0.00
			$u_c(f) = \sqrt{\Sigma\, u_i^{\,2}(f)}$	1.73 μm
			k=2 expanded uncertainty $U(f)$	3.46 μm

Table 27. Budget for measurement 5

Component x_i	Mean $(\bar{x}_i)$	Standard uncertainty $u(x_i)$	Sensitivity coefficient $c_i = \partial f / \partial x_i$	Uncertainty contribution $u_i(f) = |c_i| u(x_i)$ μm
r_1	2.60 m	0.16 μm	-1.00	0.16
r_2	5.17 m	1.29 μm	1.00	1.29
θ_1	-1.07 rad	8.74 μrad	0.00	0.00
$d\theta_2$	0.00 rad	0.48 μrad	0.00	0.00
$\emptyset_1$	1.71 rad	8.74 μrad	-0.00	0.00
$d\emptyset_2$	-0.00 rad	0.50 μrad	-0.00	0.00
R	2.56 m	1.28 μm	-1.00	1.28
T	22.42 $^{\circ}$C	0.52 $^{\circ}$C	-0.00	1.24
P	747.97 mm Hg	0.11 mm Hg	0.00	0.10
RH	0.18	0.05	-0.00	0.13
V_p	20.34 mm Hg	0.53 mm Hg	-0.00	0.01
K_t	0.93 x 10^{-6}	10^{-10}	-6.19	0.00
K_p	0.36 x 10^{-6}	10^{-10}	-30.83	0.00
K_h	0.05 x 10^{-6}	10^{-10}	16.04	0.00
			$u_c(f) = \sqrt{\Sigma \, u_i^2(f)}$	2.21 μm
			k=2 expanded uncertainty $U(f)$	4.42 μm

Table 28. Budget for measurement 6

Component x_i	Mean $(\bar{x}_1)$	Standard uncertainty $u(x_i)$	Sensitivity coefficient $c_i = \partial f / \partial x_i$	Uncertainty contribution $u_i(f) = |c_i|u(x_i)$ μm
r_1	2.60 m	0.11 μm	-1.00	0.11
r_2	5.67 m	1.56 μm	1.00	1.56
θ_1	-1.07 rad	8.73 μrad	0.00	0.00
$d\theta_2$	0.00 rad	0.43 μrad	0.00	0.00
$\emptyset_1$	1.71 rad	8.73 μrad	-0.00	0.00
$d\emptyset_2$	-0.00 rad	0.32 μrad	-0.00	0.00
R	3.07 m	1.54 μm	-1.00	1.54
T	22.23 $^\circ$C	0.51 $^\circ$C	-0.00	1.47
P	748.02 mm Hg	0.11 mm Hg	0.00	0.12
RH	0.18	0.05	-0.00	0.15
V_p	20.11 mm Hg	0.52 mm Hg	-0.00	0.01
K_t	0.93 x 10^{-6}	10^{-10}	-6.83	0.00
K_p	0.36 x 10^{-6}	10^{-10}	-36.76	0.00
K_h	0.05 x 10^{-6}	10^{-10}	19.37	0.00
			$u_c(f) = \sqrt{\Sigma\, u_i^{\,2}(f)}$	2.65 μm
			k=2 expanded uncertainty $U(f)$	5.30 μm

Table 29. Budget for measurement 7

Component x_i	Mean $(\bar{x}_1)$	Standard uncertainty $u(x_i)$	Sensitivity coefficient $c_i = \partial f/\partial x_i$	Uncertainty contribution $u_i(f) = |c_i|u(x_i)$ μm
r_1	2.60 m	0.21 μm	-1.00	0.21
r_2	6.11 m	1.76 μm	1.00	1.76
θ_1	-1.07 rad	8.73 μrad	0.00	0.00
$d\theta_2$	0.00 rad	0.36 μrad	0.00	0.00
$\emptyset_1$	1.71 rad	8.74 μrad	-0.00	0.00
$d\emptyset_2$	-0.00 rad	0.78 μrad	-0.00	0.00
R	3.51 m	1.76 μm	-1.00	1.76
T	22.03 $^{\circ}$C	0.51 $^{\circ}$C	-0.00	1.65
P	748.16 mm Hg	0.11 mm Hg	0.00	0.14
RH	0.18	0.05	-0.00	0.17
V_p	19.87 mm Hg	0.51 mm Hg	-0.00	0.02
K_t	0.93 x 10^{-6}	10^{-10}	-7.13	0.00
K_p	0.36 x 10^{-6}	10^{-10}	-41.51	0.00
K_h	0.05 x 10^{-6}	10^{-10}	22.19	0.00
			$u_c(f) = \sqrt{\Sigma u_i^2(f)}$	3.00 μm
			k=2 expanded uncertainty $U(f)$	6.00 μm

Table 30. Budget for measurement 8

Component x_i	Mean $(\bar{x}_1)$	Standard uncertainty $u(x_i)$	Sensitivity coefficient $c_i = \partial f / \partial x_i$	Uncertainty contribution $u_i(f) = |c_i| u(x_i)$ μm
r_1	2.60 m	0.15 μm	-1.00	0.15
r_2	6.56 m	1.98 μm	1.00	1.98
θ_1	-1.07 rad	8.73 μrad	0.00	0.00
$d\theta_2$	0.00 rad	0.49 μrad	0.00	0.00
$\emptyset_1$	1.71 rad	8.75 μrad	-0.00	0.00
$d\emptyset_2$	-0.00 rad	0.56 μrad	-0.00	0.00
R	3.95 m	1.98 μm	-1.00	1.98
T	22.36 $^\circ$C	0.51 $^\circ$C	-0.00	1.86
P	748.18 mm Hg	0.11 mm Hg	0.00	0.15
RH	0.18	0.05	-0.00	0.20
V_p	20.27 mm Hg	0.51 mm Hg	-0.00	0.02
K_t	0.93 x 10^{-6}	10^{-10}	-9.32	0.00
K_p	0.36 x 10^{-6}	10^{-10}	-46.70	0.00
K_h	0.05 x 10^{-6}	10^{-10}	25.09	0.00
			$u_c(f) = \sqrt{\Sigma\, u_i^{\,2}(f)}$	3.37 μm
			k=2 expanded uncertainty $U(f)$	6.74 μm

APPENDIX B: TEMPERATURE PROBE CALIBRATION

This section brings out more information on the calibration of the individual temperature probes used for thermal compensation. A total of 8 temperature probes were calibrated using the methods described in the ITS-90 [6]. However, as described in section 3.4 of this thesis, the temperature points defined in the ITS-90 standard were not used. Instead, a metrology well was used to calibrate the probes at temperatures close to room temperature (25 °C).

For the range of 13.8033 K (triple point of equilibrium hydrogen) to 961.78 °C (freezing point of silver), the temperature points of the ITS-90 scale (or T_{90} points) are defined by a platinum resistance thermometer calibrated at specified sets of fixed points, and using specified reference and deviation functions.

The standard makes use of resistance ratios, which are the ratios of resistance $R(T_{90})$ at a temperature T_{90} and the resistance $R(273.16 \text{ K})$ at the triple point of water. The observed value of this resistance ratio, $W(T_{90})$ is compared to the ideal reference ratio $W_r(T_{90})$ calculated using appropriate reference function. The difference between these observed and ideal resistance ratios is then expressed in terms of probe coefficients using appropriate deviation functions specified in the standard.

For the sub-range 0 °C - 29.7646 °C (melting point of gallium), the standard requires only one calibration point other than the triple point of water, namely 29.7646 °C. Also, for this sub-range, only one probe coefficient (a) is determined in the calibration

process. Table 31 shows the resistance ratios and probe coefficients calculated for each probe.

Table 31. Calculation of probe coefficients

Probe number	Temperature T (°C)	Resistance R (Ω)	Observed resistance ratio W	Reference resistance ratio W_r	Probe coefficient $a = \frac{W - W_r}{W - 1}$
1	25.012	109.53	1.0953	1.0993	-0.0420
2	25.009	109.73	1.0973	1.0993	-0.0204
3	25.010	109.75	1.0975	1.0993	-0.0192
4	25.008	109.70	1.0970	1.0993	-0.0244
5	25.010	109.74	1.0974	1.0993	-0.0204
6	25.009	109.75	1.0975	1.0993	-0.0189
7	25.009	109.70	1.0970	1.0993	-0.0238
8	25.008	109.65	1.0965	1.0993	-0.0293

The probe coefficients thereby obtained were then entered into the temperature-probe-controller using its 'Cal' mode and selecting ITS-90 as the desired method of input of probe coefficients. More information on how this information can be entered, can be found in the manual for the controller.

APPENDIX C: REFERENCE LASER COMPENSATION

In absence of an environmental compensation module for a laser interferometer, environmental data from sensors can be used to achieve compensation via the following equation obtained from the non-mandatory appendix H of ASME B5.57.1998: Laser and machine scale corrections.

$$CLR = LDR \left[1 + K_t(T_s - 20) - K_p(P_s - 760) + K_h(V_s - 10)\right]$$

where

CLR = Corrected Laser Reading

LDR = Laser Display Reading

K_t = Coefficient of refractive index change due to temperature, 0.96 x 10^{-6}/°C

K_p = Coefficient of refractive index change due to pressure, 0.36 x 10^{-6}/mm Hg

K_h = Coefficient of refractive index change due to humidity, 0.05 x 10^{-6}/ mm Hg

T_s = Mean air temperature, °C

P_s = Air pressure, mm Hg

V_s = Partial pressure of water vapor, mm Hg

It is to be noted that the above equation can be used only if the laser display reading (LDR) represents the laser reading compensated for standard air (20 °C temperature, 760 mm Hg pressure and 50% relative humidity), as was the case.